PAPER

Photocatalytic performance, anti-bacterial activities and 3-chlorophenol sensor fabrication using MnAl$_2$O$_4$·ZnAl$_2$O$_4$ nanomaterials†

Md Abdus Subhan, [ID] *[a] Pallab Chandra Saha, [ID] [a] Anwar Hossain, [ID] [a] Abdullah M. Asiri,[bc] M. M. Alam, [ID] [d] Mohammad Al-Mamun, [ID] [e] William Ghann,[f] Jamal Uddin, [ID] [f] Topu Raihan,[g] A. K. Azad[g] and Mohammed M. Rahman*[bc]

A MnAl$_2$O$_4$·ZnAl$_2$O$_4$ nanomaterial was synthesized by co-precipitation and characterized by XRD, SEM, EDS, TEM, AFM, FTIR, PL, CV and EIS. The photocatalytic activity of the nanocomposite against MV dye and its MDR anti-bacterial functions were studied. The nanocomposite shows excellent photocatalytic as well as anti-bacterial activity. A MnAl$_2$O$_4$·ZnAl$_2$O$_4$ nanomaterial/Nafion/GCE electrode was fabricated and implemented as the working electrode of a 3-CP sensor. The sensor exhibited good sensitivity, with the lowest detection limit, fast response time, large linear dynamic range (LDR), and long-term stability in the chemical environment. The estimated sensitivity is 70.07 μA mM^{-1} cm^{-2}. The LDR, limit of detection (LOD), and limit of quantification (LOQ) are 0.1 nM to 0.01 M, 0.0014 ± 0.0001 nM, and 0.004 nM, respectively. The MnAl$_2$O$_4$·ZnAl$_2$O$_4$ nanomaterial/Nafion/GCE is a promising fabricated sensor probe for the selective detection of 3-CP for the environmental safety and healthcare fields on a large scale.

Introduction

Mixed metal oxides are known as promising catalysts due to their excellent properties, including stability, wide range selectivity, high recovery efficiency and suitable energy band structures. Their optical properties and catalytic activity are significant.[1–6] Manganese oxide (MnO) nanoparticles have biological applications, including drug delivery and imaging. Manganese oxides, including MnO, MnO$_2$, Mn$_2$O$_3$ and Mn$_3$O$_4$, are attractive oxide materials and have been used in wastewater treatment, catalysis, sensors, supercapacitors, and rechargeable batteries.[7] These manganese oxide nanomaterials have

attracted attention as anode materials in lithium-ion batteries for their high capacity, low cost, environmental generosity, etc.[7]

Zinc oxide (ZnO) nanoparticles are an attractive material with distinctive properties, such as high sensitivity, large specific surface area, non-toxicity and high isoelectric points. ZnO is a stable n-type semiconducting material with wide applications, including luminescent materials, supercapacitors, batteries, solar cells, photo-catalysis, bio-sensors, and biomedical and biological applications. The nanosized materials also exhibit higher dissolution rates as well as higher solubility.[8]

Aluminum oxide is an important material that is usually used as a catalyst support due to its thermochemical steadiness in various environments and media. Al$_2$O$_3$ polycrystalline fibers and whiskers are used as strengtheners in high-temperature compositions owing to their high elastic moduli and thermochemical stability.[9] To synthesize those catalysts, a wide range of cost-effective, facile, and controllable methods have been used for a long time.[10] The catalysts derived from hydroxycarbonate precursors produced by the coprecipitation of divalent (for example, Mn, Zn) and trivalent (for example, Al) metal ion produced well-dispersed mixed metal oxides with high surface areas and small crystallites of fairly uniform size.[11] As a result, they can offer better catalytic activity.[12,13]

With the development of new characterization techniques, the catalytic study of mixed metal oxides (MMOs) has gained major interest. One of the main reasons behind this is the wide variety of applications found for MMOs.[14,15] In this study, two divalent metals (Mn, Zn) were introduced with one trivalent metal (Al), and their synthesized carbonate precursors on

aDepartment of Chemistry, Shahjalal University of Science and Technology, Sylhet 3114, Bangladesh. E-mail: subhan-che@sust.edu

bDepartment of Chemistry, Faculty of Science, King Abdulaziz University, P.O. Box 80203, Jeddah 21589, Saudi Arabia. E-mail: mmrahman@kau.edu.sa

cCenter of Excellence for Advanced Materials Research (CEAMR), King Abdulaziz University, P. O. Box 80203, Jeddah 21589, Saudi Arabia

dDepartment of Chemical Engineering and Polymer Science, Shahjalal University of Science and Technology, Sylhet 3114, Bangladesh

eCentre for Clean Environment and Energy, Griffith School of Environment, Gold Coast Campus, Griffith University, QLD 4222, Australia

fCenter for Nanotechnology, Department of Natural Sciences, Coppin State University, Baltimore, MD 21216, USA

gDepartment of Genetic Engineering and Biotechnology, Shahjalal University of Science and Technology, Sylhet 3114, Bangladesh

† Electronic supplementary information (ESI) available. See DOI: 10.1039/d1na00627d

calcination were converted to a self-assembled $MnAl_2O_4 \cdot ZnAl_2O_4$ nanomaterial. Thus, in light of the variety of crucial applications of MnO_x, Al_2O_3 and ZnO, we anticipated that a composite fabrication comprising all these single metal oxides would have excellent electronic properties and better performance as a photocatalyst, multi-drug resistant (MDR) anti-bacterial agent and electro-chemical sensor. Herein, the resulting nanocomposite $MnAl_2O_4 \cdot ZnAl_2O_4$ has been utilized as photocatalyst for methyl violet 6b (MV) dye degradation as well as for killing MDR pathogenic bacteria.

Chlorinated organic compounds have high toxicity, including estrogenic, mutagenic and carcinogenic effects.[16] Chlorinated organic compounds are discharged as waste effluent in the environment from various industrial activities, such as pharmaceuticals, pesticides, fungicides and insecticides, and they pose a long-term threat to ecological systems and humans.[17,18] Exposure to chlorophenols (CPs) causes irritation in the respiratory tract and has measurable effects on the eyes and mucous membranes. Thus, the US Environmental Protection Agency (EPA) has listed CPs as priority environmental pollutants.[19] Because CPs have a serious risk of long-term harmful effects to humans as well as the environment, urgent initiatives should be taken to establish a sustainable detection method. There are several recognized analytical methods to detect CPs, such as electrochemical methods,[20–22] gas chromatography,[23] high performance liquid chromatography (HPLC),[24] UV spectrophotometry,[25] and capillary electrophoresis (CE).[26] Among these instrumental analytical methods, the electrochemical method has great advantages, such as low cost, faster response, simple instrumentation, portability, and precise selectivity with high sensitivity and long-term stability in chemical environments.[27]

The aim of this study is to prepare an efficient chemical sensor with high selectivity and good sensitivity to detect 3-chlorophenol (3-CP) in aqueous medium by a reliable I–V method. To achieve the goal, a slurry of $MnAl_2O_4 \cdot ZnAl_2O_4$ nanomaterial was prepared and used to coat a thin layer on glassy carbon electrode (GCE) with Nafion as a conducting binder, and the resultant modified GCE acted as the working electrode of the proposed 3-CP chemical sensor to successively detect 3-CP in neutral buffer medium by an electrochemical method. The sensitivity and detection limit of the proposed chemical sensor were calculated from the slope of the calibration curve. Furthermore, the newly developed 3-CP chemical sensor revealed long-term stability, selectivity, sensitivity, reproducibility, and reusability as well as fast response.
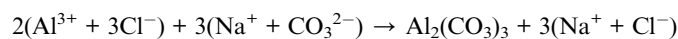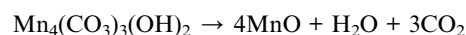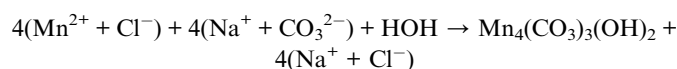
Experimental section
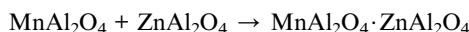
Materials and methods

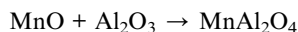$AlCl_3 \cdot 6H_2O$ (Sigma Aldrich, Germany), $MnCl_2$ (Sigma Aldrich, Germany), $Zn(NO_3)_2 \cdot 6H_2O$ (MERCK, India), Na_2CO_3 (AR, BDH) were purchased and used as supplied. All of these analytical grade chemicals were used without any further purification. As a part of this study, reagent grade chemicals such as 2,4-DNP (2,4-dinitrophenol), 2-NP (2-nitrophenol), 3-CP, 3-MP (3-methoxyphenol), 3-MPHyd (3-

methoxyphenylhydrazine), 4-NP (4-nitrophenol), 4-AP (4-aminophenol), BPA (bisphenol A), PHyd (phenylhydrazine), p-NP (p-nitrophenol), Nafion suspension (5% ethanolic solution), monosodium phosphate and disodium phosphate were procured from the Sigma-Aldrich company and used directly as received. The crystal phases and relevant structural properties of the materials were characterized using X-ray diffraction (XRD, Bruker D8 Advance diffractometer equipped with a graphite monochromator). Diffraction patterns were measured in step scan mode at 0.05 steps and at a measurement rate of 10 s per step, and they were recorded within the 2θ angle range from $10°$ to $80°$. The surface morphologies and nano-structured features were studied with an atomic force microscope (AFM, NaioAFM, NanoSurf), and a scanning electron microscope (SEM) equipped with energy dispersive X-ray spectroscopy (EDS, JSM-7100F) linked with an EDS mapping device (Oxford). The transmission electron microscopy (TEM) images were obtained by a JEOL JEM-1400 series 120 kV. The Fourier transform infrared spectroscopy (FTIR) analysis of the samples was carried out using a FTIR spectrometer (Shimadzu, FTIR-8400S). Photoluminescence (PL) of the nanocomposite was investigated by a spectro-flurophotometer (Shimadzu Corp. model RF-5301), and the photocatalytic performance was studied with a double beam UV-visible spectrophotometer (UV-1800 series, Shimadzu Corporation, Kyoto, Japan). The current *versus* potential (I–V) method was implemented in the potential range of 0–1.5 V using a Keithley electrometer (6517A, USA) at room conditions.

Preparation of $MnAl_2O_4 \cdot ZnAl_2O_4$ nanomaterials

A simple and low-cost co-precipitation method was used to synthesize the $MnAl_2O_4 \cdot ZnAl_2O_4$ nanocomposite. Solutions of 0.25 M, $AlCl_3 \cdot 6H_2O$, $MnCl_2$, and $Zn(NO_3)_2 \cdot 6H_2O$, which acted as sources of aluminum, manganese and zinc, respectively, were prepared in aqueous medium. These metal salt solutions were added to a beaker (50 mL each) and stirred continuously for 15 minutes. To this mixture, 0.5 M Na_2CO_3 solution was added dropwise until completion of the reaction at 45 °C. The resulting mixture was stirred continuously for 1 further hour at 45 °C. After accomplishment of the reaction, the white precipitate was isolated from the solution by centrifugation and washed several times with deionized water. The precipitate was dried at 120 °C in an oven for 2.5 hours. The white precipitate obtained was crushed in a mortar and calcined in an electric muffle furnace (Gallenkamp, Korea) at 650 °C for 4 h. The metal carbonates were converted to their corresponding oxides through calcination.[28] The overall reactions can be summarized as below:
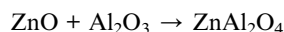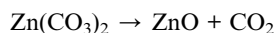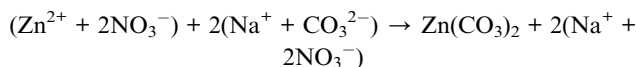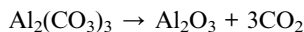
$$4(Mn^{2+} + Cl^-) + 4(Na^+ + CO_3{}^{2-}) + HOH \rightarrow Mn_4(CO_3)_3(OH)_2 + 4(Na^+ + Cl^-)$$

$$Mn_4(CO_3)_3(OH)_2 \rightarrow 4MnO + H_2O + 3CO_2$$

$$2(Al^{3+} + 3Cl^-) + 3(Na^+ + CO_3{}^{2-}) \rightarrow Al_2(CO_3)_3 + 3(Na^+ + Cl^-)$$

$$Al_2(CO_3)_3 \rightarrow Al_2O_3 + 3CO_2$$

$$(Zn^{2+} + 2NO_3^-) + 2(Na^+ + CO_3^{2-}) \rightarrow Zn(CO_3)_2 + 2(Na^+ + 2NO_3^-)$$

$$Zn(CO_3)_2 \rightarrow ZnO + CO_2$$

$$MnO + Al_2O_3 \rightarrow MnAl_2O_4$$

$$ZnO + Al_2O_3 \rightarrow ZnAl_2O_4$$

$$MnAl_2O_4 + ZnAl_2O_4 \rightarrow MnAl_2O_4 \cdot ZnAl_2O_4$$

Corresponding bi-metal and mono-metal oxide nanomaterials were synthesized with the same procedure.

Fabrication of GCE with $MnAl_2O_4 \cdot ZnAl_2O_4$ nanomaterial

The synthesized nanomaterial was used to make a slurry with ethanol and subjected to coating as a thin layer on GCE. The modified GCE (radius of the sensing area is 0.1 cm; surface area is 0.0316 cm^2) was dried in room conditions. To improve the stability of the working electrode of the chemical sensor, a drop of 5% Nafion suspension was added to the GCE, which increased the binding strength between the nanomaterials and GCE. The fabricated probe was maintained in an oven at 34 °C. The constructed electrochemical cell was mounted with $MnAl_2O_4 \cdot ZnAl_2O_4$ nanomaterial/Nafion/GCE and Pt-wire (dia., 1.5 mm), where $MnAl_2O_4 \cdot ZnAl_2O_4$ nanomaterial/Nafion/GCE functioned as the working electrode and Pt-wire was used as the counter electrode. Several solutions based on the concentration range (0.1 nM to 0.1 M) of 3-CP were made as well and utilized as the target analyte. The sensitivity of the proposed sensor probe was analyzed from the slope of the calibration curve, which is the current *versus* the concertation of the 3-CP plot at the applied potential of +1.5 V. The LDR and DL were computed from the calibration curve at a signal to noise ratio equal to 3. The experimental setup was a simple two-electrode system. The amount of 0.1 M PBS was kept constant in the cell as 10.0 mL during the experiment.

Results and discussion

Structural characterization of $MnAl_2O_4 \cdot ZnAl_2O_4$ nanomaterials

The X-ray diffraction pattern of the synthesized nanoparticles showed similarities with JCPDS files no 29-0880 and 74-1138. The peaks observed at 2θ values of 30.653° (2 2 0), 36.400° (3 1 1), 64.368° (4 4 0), and 72.869° (6 2 0) have similarities with JCPDF file #29-0880, and this appears to be the $MnAl_2O_4$ structure (Fig. 1). It has a cubic (*Fd3m*) shape with a lattice parameter ($a = b = c$) of 8.204 Å. The peaks found with the 2θ values of 31.21° (2 2 0), 38.472° (2 2 2), 55.541° (4 2 2), 59.234° (5 1 1), and 68.481° (5 3 1) can be assigned to $ZnAl_2O_4$ (JCPDF #74-1138). The $ZnAl_2O_4$ also shows a cubic (*Fd3m*) structure with a lattice parameter ($a = b = c$) of 8.099 Å. As can be seen in Fig. 1, some of the XRD peaks are not sharp. This is because of
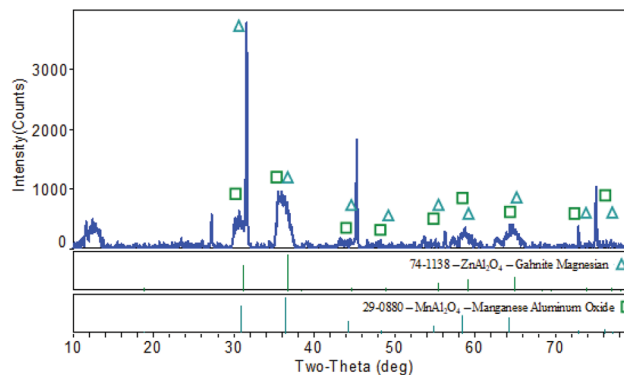

Fig. 1 X-ray diffraction pattern of the $MnAl_2O_4 \cdot ZnAl_2O_4$ nanomaterial.

overlap of the different peaks originating from different metal oxides due to the formation of the mixed metal oxide nanocomposite. The crystallite size of the $MnAl_2O_4 \cdot ZnAl_2O_4$ nanocomposite was calculated from the XRD data using Scherrer's formula, $\tau = K\lambda/(\beta \cos \theta)$, where τ is the mean size, K is a dimensionless shape factor with a value of 0.94, λ is the X-ray wavelength (0.1506 nm), β is the line broadening at half the maximum intensity (FWHM) and θ is the Bragg angle.[28] A set of data obtained from the XRD measurements was used for calculating the crystallite size, which was found to be 48.5 nm.

SEM-EDS analysis of the $MnAl_2O_4 \cdot ZnAl_2O_4$ nanomaterial

SEM analysis was performed to determine the surface morphology of the $MnAl_2O_4 \cdot ZnAl_2O_4$ nanomaterial (Fig. 2). With higher magnification of 80 000×, as shown in Fig. 2(a), a structure with different crystals is revealed. Some platelike (somewhat long) morphologies are observed with smaller particles on their surfaces, as shown in Fig. 2(a). However, at low magnification (19 000×), as shown in Fig. 2(b), 3D flower-like structures were observed that are dispersed on the surface with a heterogeneous morphology.

EDS analysis of the $MnAl_2O_4 \cdot ZnAl_2O_4$ nanomaterial (Fig. 2(c)) was carried out, and elemental mapping was performed to determine the distribution of the composition in the matrix. As shown in Fig. 2(c) and Table S1,† the NPs are composed of Al, Mn, Zn and O with atomic percentages of 20.32%, 7.93%, 24.34%, and 47.4%, respectively. The peak that appeared at ~1.74 is an artifact (from Si Kα) and that observed at ~2.62 may be due to the traces of Cl from the starting materials used in the synthesis of the nanocomposite. Furthermore, SEM-EDS mapping (Fig. S1†) showed that elements were not restricted in a confined space; rather, they are dispersed throughout the matrix.

TEM study of the $MnAl_2O_4 \cdot ZnAl_2O_4$ nanomaterial

For further insight into the surface and morphology of the $MnAl_2O_4 \cdot ZnAl_2O_4$ nanomaterial, a TEM study was performed. Almost uniformly sized particles in agglomerated form were observed by TEM (Fig. 3(a)). Small plate-like morphology of the particles was observed by TEM. When Mn is combined with Al
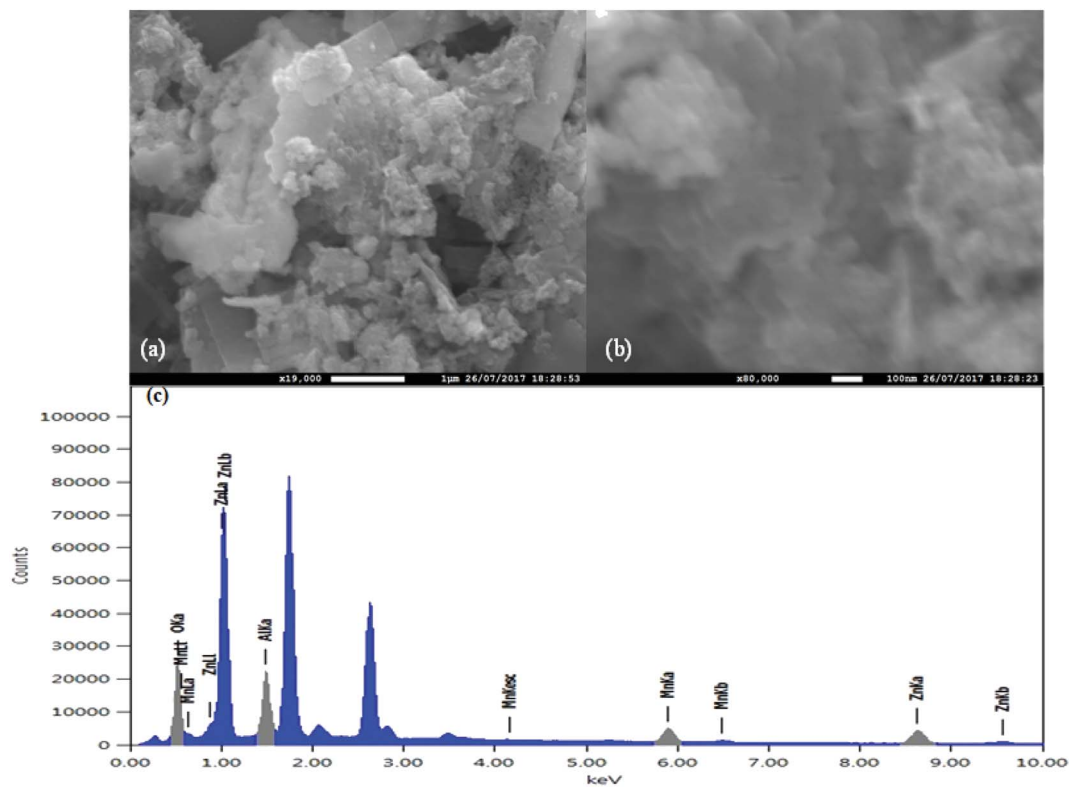
Fig. 2 Surface analysis: (a) low magnified and (b) high magnified image of the $MnAl_2O_4 \cdot ZnAl_2O_4$ nanomaterial and (c) EDS of the $MnAl_2O_4$-$\cdot ZnAl_2O_4$ nanomaterial.

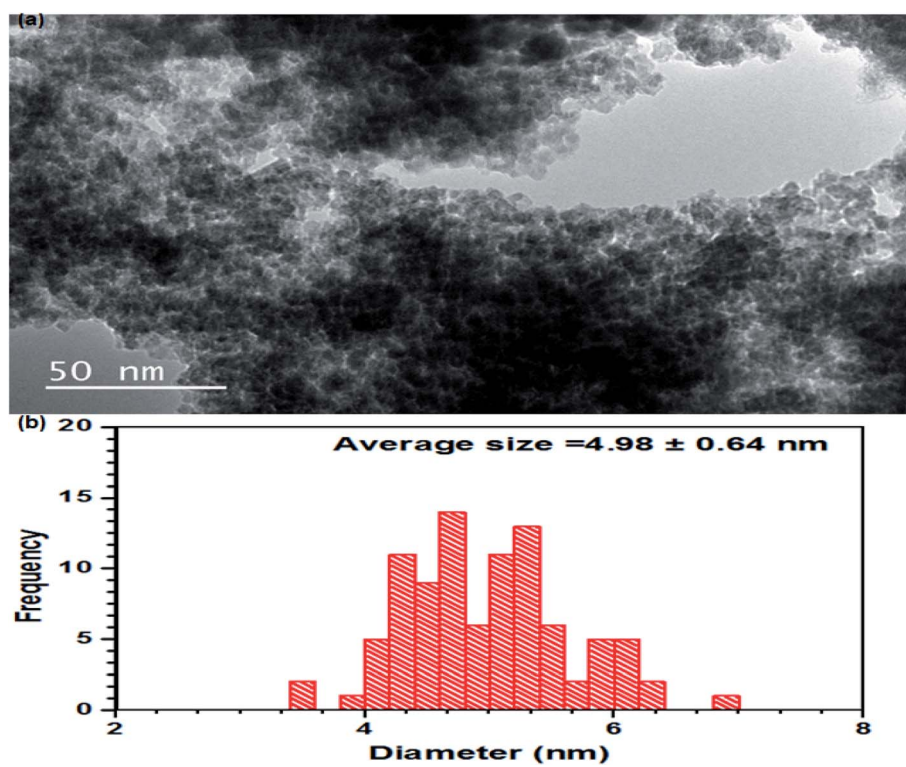**Fig. 3** Transmission electron microscope image of the $MnAl_2O_4 \cdot ZnAl_2O_4$ nanomaterial (a) and particle size (b).

and Zn, the resulting composite is highly magnetic. Because of the high aggregation of the nanomaterial resulting from these magnetic interactions, the particles are not clearly distinct by TEM. The average particle size measured by TEM is ~5 nm, as shown in Fig. 3(b).

Atomic force microscopy of the $MnAl_2O_4 \cdot ZnAl_2O_4$ nanomaterial

AFM of the $MnAl_2O_4 \cdot ZnAl_2O_4$ nanomaterial was performed by making a thin film on a glass slide and dispersing the nanomaterial in acetone by ultrasonication. A silicon carbide cantilever was used, and data were acquired in dynamic tapping mode. The image shown in Fig. S2† indicates particle dimensions of 200×118 nm. The height profile of the $MnAl_2O_4 \cdot ZnAl_2O_4$ nanomaterial film surface was recorded; the feature height of the film is close to 20 nm, as shown in Fig. S3.†

IR spectroscopic investigation of $MnAl_2O_4 \cdot ZnAl_2O_4$ nanomaterial

The IR spectrum of the $MnAl_2O_4 \cdot ZnAl_2O_4$ nanomaterial was taken to investigate the modes of M–O interactions. The low wave number regional bands at $400–850$ cm^{-1} may correspond to the vibration modes of M–O and O–M–O (M = Al, Mn, Zn) (Fig. S4†). The bands at 1379 cm^{-1} may be due to antisymmetric stretching vibrations of CO_3^{2-}. The IR band at around 1043 cm^{-1} may be due to the C–O single bond stretching mode. These may be due to the presence of traces of CO_3^{2-} in the compound. The broad absorption band at 3454 cm^{-1} is due to the presence of the O–H stretching mode of hydroxyl groups of adsorbed water from the environment. The peak at 1641 cm^{-1} may be due to H–O–H bending vibration of water. The vibrations of Zn–O were observed at 485, 497 and 543 cm^{-1}. The IR band at around 600 cm^{-1} may be due to Al–O stretching vibrations and that at 667 cm^{-1} may be due to Al–O–Al stretching vibrations. The IR peaks at 700 and 750 cm^{-1} may be due to Mn–O and Mn–O–Mn vibrations, respectively.[29–31]

Photoluminescence properties of the $MnAl_2O_4 \cdot ZnAl_2O_4$ nanomaterial

To observe the PL activity of various metal oxides, the tri-metal oxide ($MnAl_2O_4 \cdot ZnAl_2O_4$) and its corresponding bi-metal and mono-metal oxide nanomaterials were synthesized with the same procedure. A comparison between the PL spectra of the tri-, bi- and mono metal oxides with an excitation energy of 230 nm is shown in Fig. 4. PL of the $MnAl_2O_4 \cdot ZnAl_2O_4$ nanomaterial (Fig. S5†) was also observed with different excitation energies. When excited at 230 nm, it showed emission peaks at 371 and 469 nm. The highest energy band observed at 371 nm is due to the near band edge (NBE) emission. Upon excitation with 350 nm light, it showed emission peaks at 405, 428 and 450 nm at almost equidistant positions. PLE was observed (Fig. S6†) by monitoring at 450 nm, and peaks were observed at 352, 368 and 388 nm.

Similarly, the PL of the bi-metallic oxides, *i.e.*, $MnAl_2O_4$, $MnO \cdot ZnO$ and $ZnAl_2O_4$, was observed at different wavelengths, as shown in Fig. 4 and S7–S9.† Moreover, the PL spectra of the
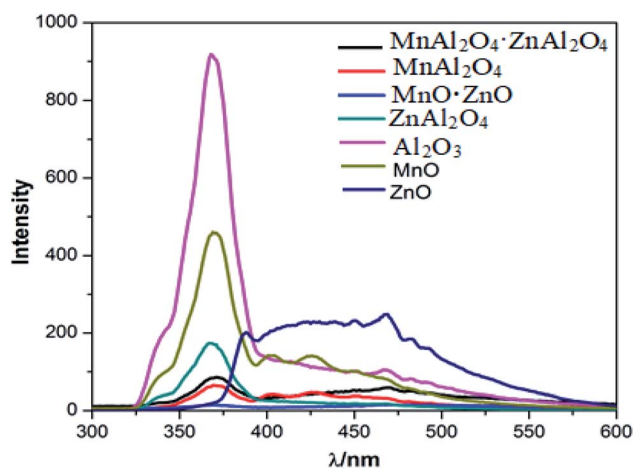

Fig. 4 Comparative PL spectra of the tri-metallic, di-metallic and mono-metallic oxide nanomaterials upon 230 nm excitation energy.

mono-metallic oxides (Al_2O_3, MnO and ZnO) were observed and are shown in Fig. 4 and S10–S12.† They showed diverse PL peaks with different luminescent centers ranging from 367 to 489 nm. In each case, the highest energy strong NBE emission band was observed at ~370 nm (367–371 nm region). All the PL peaks are compiled in Table S2.† As executed in Fig. 4, the PL peaks, patterns and intensities of the $MnAl_2O_4 \cdot ZnAl_2O_4$ nanomaterial are different from those of the bi-metallic as well as the mono metal oxides. The PL intensity of $MnAl_2O_4 \cdot ZnAl_2O_4$ is reduced in general compared to that of the monometallic or bi-metallic oxides. These PL results indicate that the recombination rate of electron–holes has been reduced markedly upon trimetallic nanostructure formation, resulting in decreased PL intensity. This decrease of the electron–hole recombination rate may have a great impact on the photocatalytic activity of the $MnAl_2O_4 \cdot ZnAl_2O_4$ nanomaterial.

Photocatalytic application of the $MnAl_2O_4 \cdot ZnAl_2O_4$ nanomaterial

Methyl violet has many medical uses; however, it is a mutagen and mitotic poison. Therefore, concerns exist regarding the ecological impact of the release of methyl violet into the environment. Methyl violet dye has been used in vast quantities for textile and paper dying, and around 15% of the MV produced world-wide is released to environment in wastewater.[32]

The photocatalytic dye degradation of methyl violet 6b (MV) solution was carried out in the presence of $MnAl_2O_4 \cdot ZnAl_2O_4$ nanomaterial with a low-pressure visible lamp of 20 W. First, a fixed portion of photocatalyst was taken in a beaker. It was mixed with the MV dye solution. Prior to visible light irradiation to evaluate the adsorption–desorption equilibrium, the mixture was stirred for about 60 minutes in the dark. The dye solution was collected at regular time intervals, and UV-visible spectra were recorded using a spectrophotometer by removing 4 mL dye solution from the reaction mixture with the photocatalyst. This experiment was performed at pH 9 and pH 7 with a catalyst dose of 0.5 g L^{-1}. H_2O_2 was used as a catalytic activity booster. The
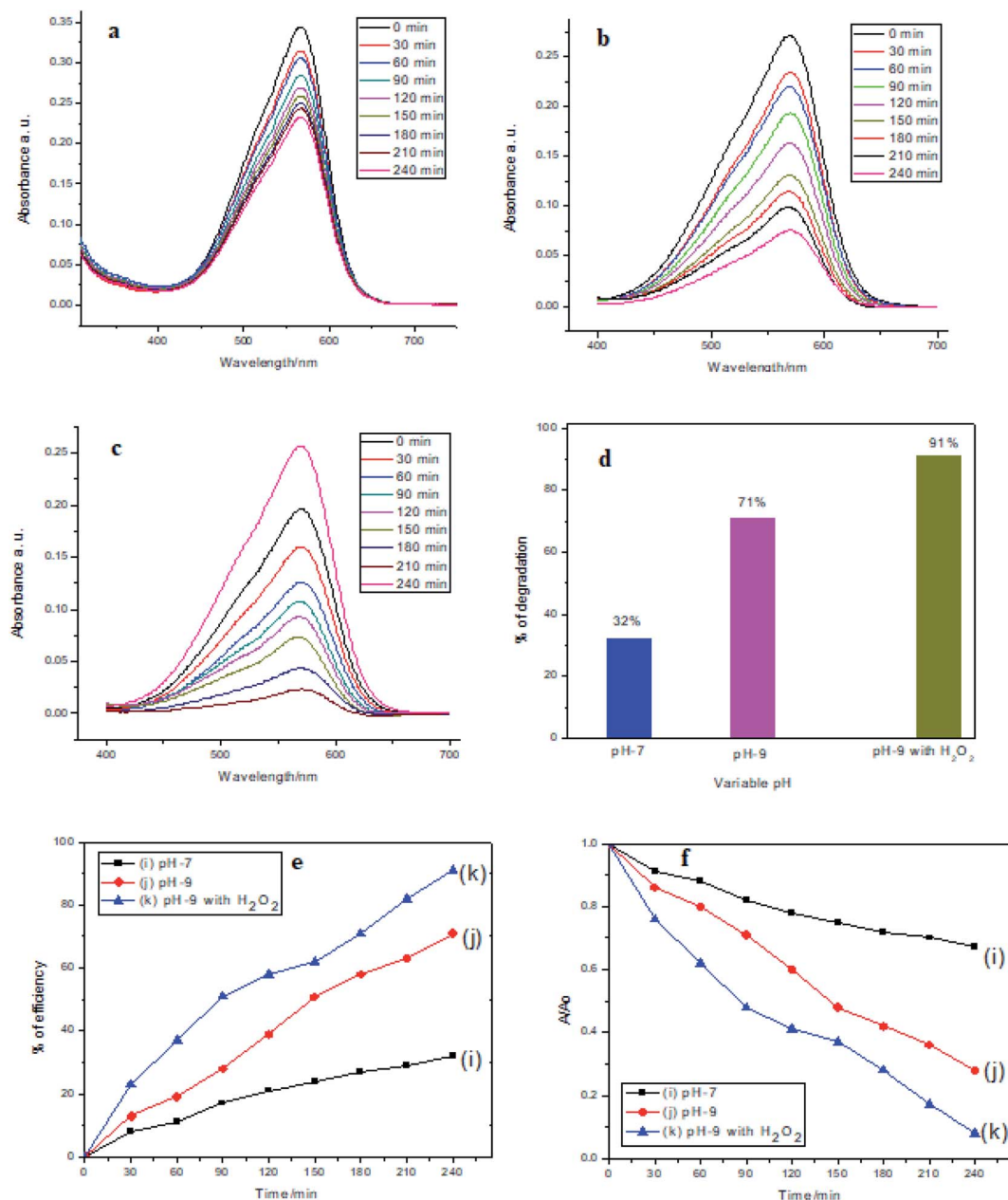
Fig. 5   Photocatalytic degradation of MV dye in the presence of the MnAl$_2$O$_4$·ZnAl$_2$O$_4$ nanomaterial at (a) pH 7, (b) pH 9, (c) pH 9 with H$_2$O$_2$ (d); % of efficiency with respect to pH (e); % of efficiency (MV concentration 5 mg L^{-1}, catalytic dosage: 0.5 g L^{-1}). (f) Degradation of dye with time.

degradation of MV dye was measured with time, and the photocatalytic efficiency Z was determined by the following equation.

$$Z = (1 \times C/C_0) \times 100 = (1 \times A/A_0) \times 100$$

where C_0 is the concentration of MV before the irradiation, C is the concentration of the MV dye at the degradation time, and A_0 and A are the corresponding absorbances.

Moreover, recovery of the catalyst MnAl$_2$O$_4$·ZnAl$_2$O$_4$ and its reuse in photocatalytic processes were evaluated using a similar process under the same experimental conditions to enable substantial reduction of the operative cost, which is

a vital parameter in photocatalyst development for wastewater treatment. Further, a kinetics study of methyl violet 6b degradation on the MnAl$_2$O$_4$·ZnAl$_2$O$_4$ nanomaterial was performed to determine the rate and order of the dye degradation reaction.

Among the MV degradation products, N-imido oxides and hydroxylamine derivates, together with their demethylated derivatives, have been determined.[33] UV-visible light leads to formation of several degradation products with loss of ˙CH$_3$, CH$_4$, CO, phenylmethylamine and phenyldimethylamine, absorbing at shorter wavelengths than MV (blue shift) or non-absorbing in the visible range (yellow-colorless), leading to
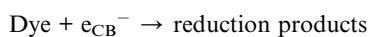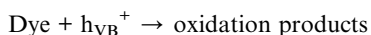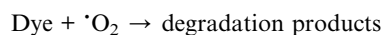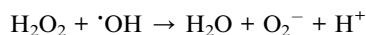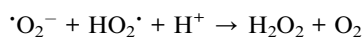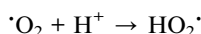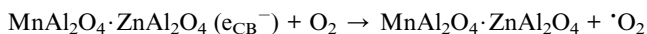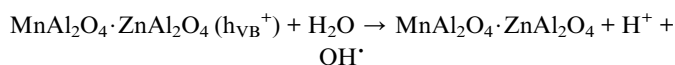
a decrease in the absorption intensity (Fig. S13†). Thus, the decrease in the absorption spectra with time was monitored to evaluate the dye degradation efficiency of the $MnAl_2O_4 \cdot ZnAl_2O_4$ nanomaterial.[33]

Photocatalytic activity of $MnAl_2O_4 \cdot ZnAl_2O_4$ nanomaterial at different pH values

Fig. 5 shows that for the catalyst at pH 7 and 9 and the catalyst at pH 9 with H_2O_2, the dye degradation efficiencies were 32%, 71% and 91%, respectively. Fig. 5(a–c) shows MV dye degradation through a gradual decrease in intensity of the absorption spectra with time. Fig. 5(d) shows the percentages of dye degradation efficiency at pH 7 and 9 by the catalyst only and at pH 9 by the catalyst with H_2O_2 in a bar diagram. Fig. 5(e) shows the % of efficiency of MV dye degradation by the catalyst only at pH 7 and 9 and by the catalyst in the presence of H_2O_2 at pH 9. Similarly, Fig. 5(f) shows the degradation of MV dye with time by the catalyst only at pH 7 and 9 and by the catalyst with H_2O_2 at pH 9.

The $MnAl_2O_4 \cdot ZnAl_2O_4$ nanocomposite, when excited by light, generates photo-excited electrons in medium. The photoexcited electrons contribute to the generation of ˙OH. This process is further accelerated by H_2O_2. In the presence of ˙OH radicals generated by oxidizing hydroxide ions in slightly basic media, the efficacy of the process is noticeably boosted at pH 9. The pH and H_2O_2 certainly have robust effects on the photodegradation of dyes. When H_2O_2 is added to the heterogeneous catalytic system, the concentration of ˙OH radicals increases. At high ˙OH concentration, the excess ˙OH is consumed by the H_2O_2, and it performs as a hydroxyl radical scavenger.[28] The ˙OH radicals degrade MV dyes to smaller, less toxic fragments. Superoxide radicals are also formed in these photocatalytic reactions, which also contributes to MV dye degradation. The proposed photocatalytic reactions can be summarized as below:[34,35]

$$MnAl_2O_4 \cdot ZnAl_2O_4 + h\nu \rightarrow MnAl_2O_4 \cdot ZnAl_2O_4 \ (e_{CB}^- + h_{VB}^+)$$

$$MnAl_2O_4 \cdot ZnAl_2O_4 \ (h_{VB}^+) + H_2O \rightarrow MnAl_2O_4 \cdot ZnAl_2O_4 + H^+ + OH˙$$

$$MnAl_2O_4 \cdot ZnAl_2O_4 \ (h_{VB}^+) + OH^- \rightarrow MnAl_2O_4 \cdot ZnAl_2O_4 + OH˙$$

$$MnAl_2O_4 \cdot ZnAl_2O_4 \ (e_{CB}^-) + O_2 \rightarrow MnAl_2O_4 \cdot ZnAl_2O_4 + ˙O_2$$

$$˙O_2 + H^+ \rightarrow HO_2˙$$

$$˙O_2^- + HO_2˙ + H^+ \rightarrow H_2O_2 + O_2$$

$$H_2O_2 + ˙OH \rightarrow H_2O + O_2^- + H^+$$

$$Dye + OH˙ \rightarrow degradation \ products$$

$$Dye + ˙O_2 \rightarrow degradation \ products$$

$$Dye + h_{VB}^+ \rightarrow oxidation \ products$$

$$Dye + e_{CB}^- \rightarrow reduction \ products$$

where $h\nu$ is the photon energy required to excite the semiconductor electron from the valence band (VB) to the conduction band (CB).

Catalytic stability of the $MnAl_2O_4 \cdot ZnAl_2O_4$ nanomaterial

The possibility of recovery of the catalyst $MnAl_2O_4 \cdot ZnAl_2O_4$ nanomaterial for reuse in photocatalytic processes is another crucial issue. This recovery and reuse contribute substantially to reducing the operative cost, which is a crucial parameter in the appropriateness of photocatalysis for wastewater treatment. The catalyst renewal process is very simple. After completing the photocatalysis, the solution was maintained for 24 h, and the supernatant was decanted. Then, the catalyst was rinsed with distilled water and dried at 120 °C for 2 hours. To assess the effectiveness of the reused photocatalyst, a series of experiments were accomplished using 0.5 g L^{-1} catalyst under visible light at pH 9 of the methyl violet 6b (dye) solution. To determine the experimental results for the stability of the photocatalyst, recycling experiments were carried out, and the results are presented in Fig. 6(a–f). Fig. 6(a–e) shows a gradual decrease in intensity of the UV-Vis spectra with time for the 1st to 5th use of the catalyst at pH 9. For each new cycle, the photocatalyst was recycled for the degradation of a fresh MV solution by filtering and drying in identical conditions. In the presence of the $MnAl_2O_4 \cdot ZnAl_2O_4$ catalyst at pH 9, the degradation percentages of MV solution for 5 cycles of use were 71%, 67%, 64%, 59% and 53% after 4 h of visible light irradiation, respectively (Fig. 6(f)). The results revealed that the catalytic function of the catalyst at pH 9 had a seeming decrease in the second use and afterward maintained relative steadiness. The adsorption of intermediate products on the photocatalyst active sites made them unreachable for degradation of fresh dye solution, which may be the cause of this reduction in the photocatalyst activity. However, 53% of MV was degraded successfully in the 5th use of the photocatalyst, which reflected the reusability of the catalyst.

Kinetics study of methyl violet 6b degradation on the $MnAl_2O_4 \cdot ZnAl_2O_4$ nanomaterial

The plot of $\ln([MV]_0/[MV])$ vs. time displayed a straight line with slope k at different pH values (Fig. 7). Fig. 7 shows that the pseudo-first order postulation defines the experimental data well. The detected dye degradation rate constant and the values of r-squared (r^2) are listed in Table 1. The best r^2 value (0.98053) was obtained for the catalyst at pH 9.

The excellent photocatalytic activity observed for $MnAl_2O_4 \cdot ZnAl_2O_4$ is due to the reduced recombination rate of electrons–holes on the trimetallic nanostructured formation, as revealed by the PL intensity. In summary, trimetallic oxide nanocomposites are promising photocatalyst materials due to the mixing of heterometals in the nanoassembly.[15,28,34–36]

Anti-bacterial activity of the $MnAlO_4 \cdot ZnAl_2O_4$ nanomaterial

Nanomaterials are being thoroughly studied as potential MDR anti-bacterial agents. The anti-bacterial activity of a material varies with different factors, including particle size.[37] The anti-bacterial effect also depends on different morphologies and
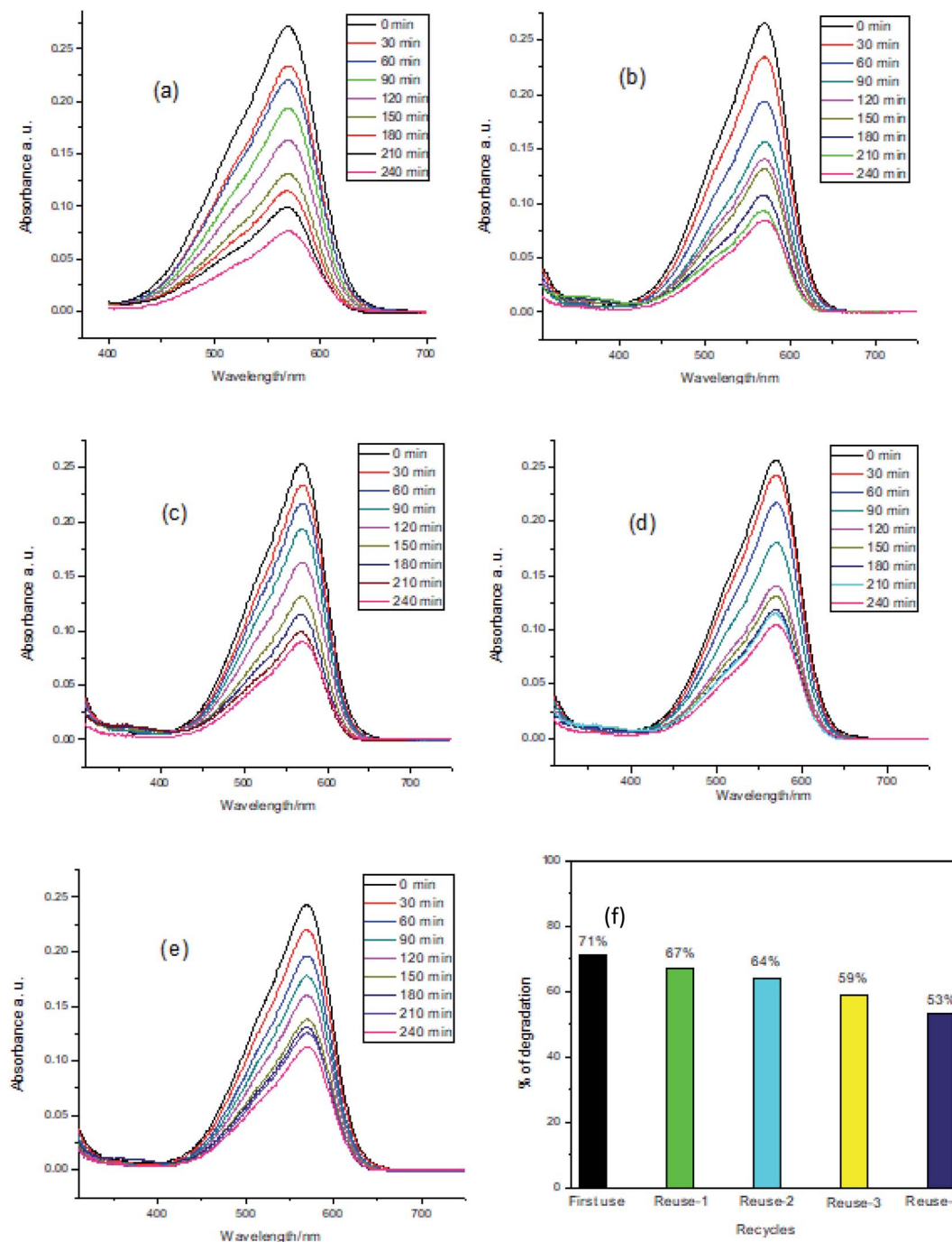
Fig. 6 Recycling and reuse of the photocatalyst for MV degradation (MV concentration: 5 mg L^{-1}), photocatalyst dosage: 0.5 g L^{-1}, in the presence of the MnAl$_2$O$_4$·ZnAl$_2$O$_4$ nanomaterial catalyst at pH 9 (a–e) and % of efficiency (f) (irradiation time 4 h).

crystal growth behaviors.[38] The anti-bacterial activities of the mixed metal oxide nanomaterial, MnAl$_2$O$_4$·ZnAl$_2$O$_4$, against some MDR infective bacteria, both Gram positive (*S. aureus*) and Gram negative (*E. coli*, *K. pneumoniae*, *P. aeruginosa*, *P. mirabilis*), were tested by the agar well diffusion method with and without light. The results are shown Fig. 8 and 9 and in Table 2.

The anti-bacterial activity of the MnAl$_2$O$_4$·ZnAl$_2$O$_4$ nanomaterial was evaluated using the agar well diffusion assay as described earlier.[39] The bacterial test organisms, namely, *E. coli*,

K. pneumoniae, *S. aureus*, *P. aeruginosa*, and *P. mirabilis*, were grown in nutrient broth overnight to attain colony-forming units (CFU) of ~1.5 × 10^8 per mL. 100 μL of each bacteria culture was spread on the nutrient agar plates according to the McFarland standard.[40] Further, an 8 mm diameter well was created at the center of each plate with the help of sterilized micropipette tips, and the wells were loaded with various concentrations of MnAl$_2$O$_4$·ZnAl$_2$O$_4$ nanomaterial solution. The plates were then incubated for 24 h at 37 °C, and the
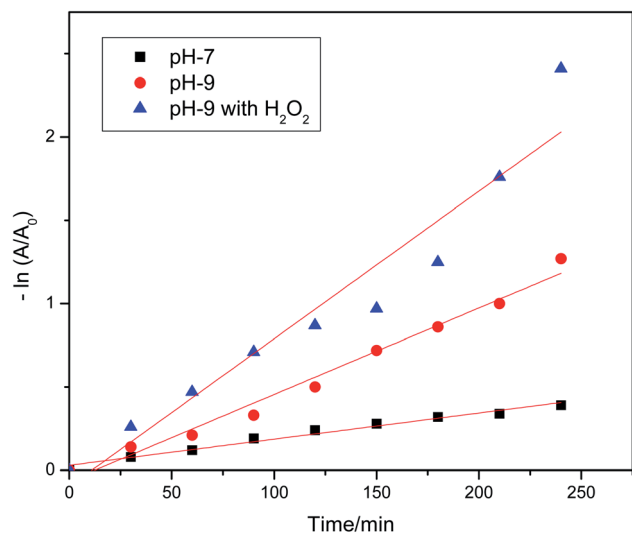
Fig. 7 Natural logarithms of absorbance of MV dye plotted as a function of visible light irradiation time. The degradation of MV dye at variable pH values by $MnAl_2O_4 \cdot ZnAl_2O_4$ nanomaterial (dosage: 0.5 g L^{-1}) in the presence of catalyst at pH 7, catalyst at pH 9, and catalyst + H_2O_2 at pH 9.

Table 1 Values of the rate constant (k) and r^2 for the dye degradation kinetics

Observation	K (min^{-1})	r^2
pH 7	0.00157	0.97756
pH 9	0.00519	0.98053
pH 9 with H_2O_2	0.00887	0.92381

diameters of the zones of inhibition were recorded in mm. The anti-bacterial activity of the $MnAl_2O_4 \cdot ZnAl_2O_4$ nanomaterial was checked both in the presence and absence of light against each bacterium in comparison with antibiotic GEN 10 as a standard.

From the clear zones of inhibition, the synthesized nanocomposite has a larger ring for all three concentrations (1 mg mL^{-1}, 2 mg mL^{-1} and 3 mg mL^{-1}) than the used GEN 10 standard, except for *P. mirabilis* (Fig. 8 and Table 2). This dominant performance of the $MnAl_2O_4 \cdot ZnAl_2O_4$ nanomaterial can be seen against all bacteria, both Gram positive and Gram negative (Fig. 8).

The effect of light on the performance of the anti-bacterial function of the synthesized nanocomposite was also studied. The effect of light on the anti-bacterial activity of $MnAl_2O_4 \cdot ZnAl_2O_4$ against each bacterium is shown in Fig. 9. It was found that in the absence of light, the $MnAl_2O_4 \cdot ZnAl_2O_4$ nanomaterial showed anti-bacterial effects in the case of all three concentrations by killing both Gram positive and Gram negative bacteria (Fig. 8). For all the cases, the activity rises as the concentration increases. However, in the presence of light (Fig. 9), all three solutions of different concentrations of $MnAl_2O_4 \cdot ZnAl_2O_4$ showed better anti-bacterial activity compared to that observed in absence of light. This is because

of the excitation of the $MnAl_2O_4 \cdot ZnAl_2O_4$ nanocomposite by light and the formation of radicals, such as reactive oxygen species (ROS), in solution, which improved the bacteria-killing through an ROS-mediated process. When irradiated with visible light, the ROS, such as superoxide radicals (${}^{\bullet}O_2^{-}$), are formed by the reactions between oxygen molecules and the photo-generated electrons (e^-) of the nanomaterial $MnAl_2O_4 \cdot ZnAl_2O_4$; these ($e^-$) moving towards the catalyst surface are found to be important for promoting the anti-bacterial activity. When the $MnAl_2O_4 \cdot ZnAl_2O_4$ nanocomposite interacts with/ penetrates the bacterial cells and becomes excited by light, the generated ROS can kill the bacterial cells and consequently enhances the antibacterial activity of the nanocomposite more than in the absence of light. The small particle size and novel structural features of the nanocomposites may also cause greater mechanical damage to the cell walls of MDR bacteria (Fig. 9 and Table 2). The results revealed the enhanced sterilizing properties of the $MnAl_2O_4 \cdot ZnAl_2O_4$ nanomaterial for industrial and biomedical applications.[28,38,39]

Determination of MIC and MBC of the $MnAl_2O_4 \cdot ZnAl_2O_4$ nanomaterial against five different bacteria

The minimum inhibitory concentration (MIC) and minimum bactericidal concentration (MBC) values were also determined for this nanocomposite against all bacteria under investigation. The MIC is defined as the lowest concentration of the antibacterial agent that inhibits the visible growth of bacteria.[41] The MIC is used to evaluate the antimicrobial efficacy of different compounds by measuring the effect of decreasing concentrations of an antibiotic or antiseptic over a definite period for inhibition of growth of a microbial population. On the other hand, the MBC is the lowest concentration of antibacterial agent that is essential to kill a bacterium over a fixed, somewhat extended period, such as 18 h or 24 h, under a specific set of conditions. The MBC can be determined from the broth dilution of MIC tests by subculturing to agar plates that do not contain the test agent. The MBC is identified by determining the lowest concentration of antibacterial agent that reduces the viability of the initial bacterial inoculum by a predetermined reduction, such as ≥99.9%.

The MIC and MBC of the $MnAl_2O_4 \cdot ZnAl_2O_4$ nanocomposite were determined using the method described in the guideline of CLSI (2012), as shown in Fig. 10 and Table 3. The MIC test was performed in a 96-well round bottom microtiter plate using standard broth microdilution methods, while the MBC test was performed on Mueller Hinton agar (MHA) plates as described previously.[37] The bacterial inoculums were grown in nutrient broth (0.5% NaCl, 0.5% peptone, 0.15% beef extract, 0.15% yeast extract; pH 7) at 37 °C in a shaker incubator (120 rpm) overnight and then adjusted to the concentration of 1.5×10^8 CFU mL^{-1}, which is comparable to McFarland standard 0.5. For the MIC test, 100 μL of the synthesized $MnAl_2O_4 \cdot ZnAl_2O_4$ nanomaterial stock solution (1 μg μL^{-1}) was added and diluted two-fold with nutrient broth (NB) starting from column 2 to column 11. Column 1 was a positive control (medium and bacterial inoculums) and column 12 was a negative control
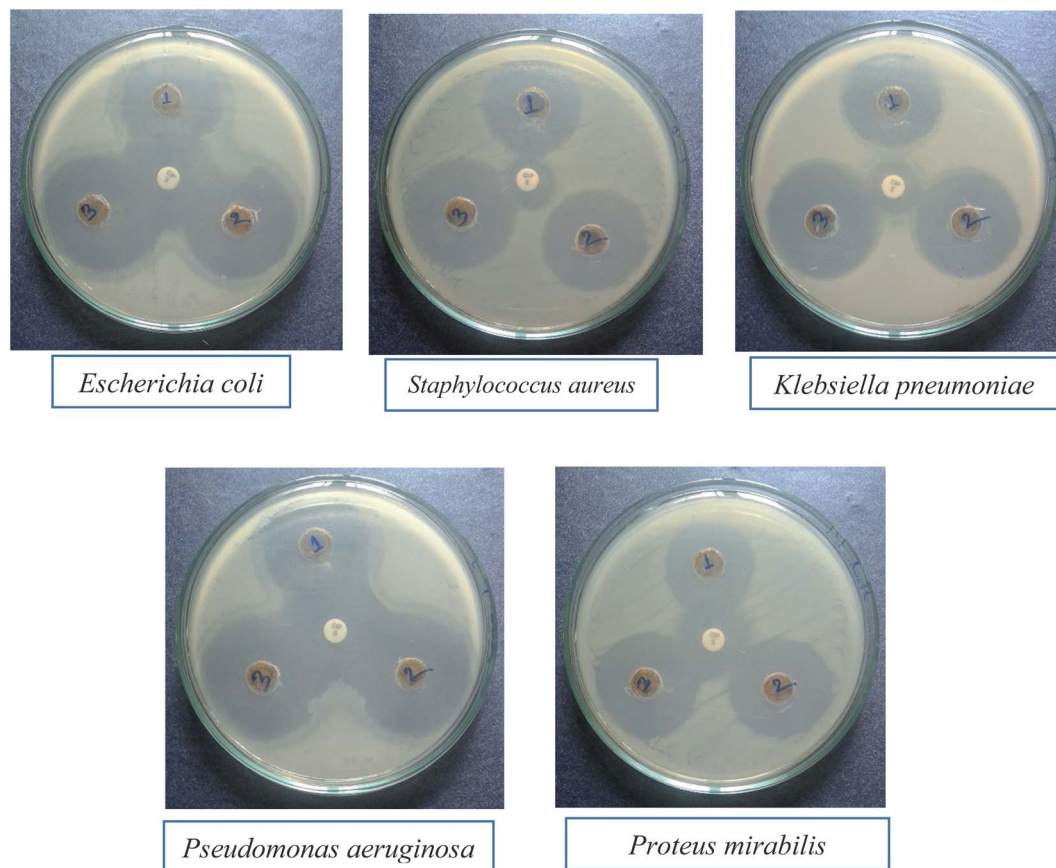
Fig. 8 *In vitro* anti-bacterial activity of the $MnAl_2O_4 \cdot ZnAl_2O_4$ nanomaterial against multidrug resistant superbugs in the absence of light (the middle spot shows the zone of inhibition by the GEN 10 standard).

(only medium) (Fig. 10). 2 μL of bacterial suspension was added to the respective wells containing $MnAl_2O_4 \cdot ZnAl_2O_4$ nanomaterial solution according to McFarland standard 0.5 and incubated at 37 °C for 24 h. After 24 h of incubation, 20 μL of PrestoBlue was added to each well and then incubated at 37 °C for 2–4 h. A blue to pink color change was due to the reduction of resazurin and, therefore, indicated bacterial growth. Similarly, a blue to pink color change showed the growth of bacteria, and the MIC was defined as the lowest concentration of the solution of $MnAl_2O_4 \cdot ZnAl_2O_4$ nanomaterial that restricted this color change. A color change of the growth control well to pink showed the appropriate growth of the isolate, and there was no color change in the sterile control well, which exhibited that it contained no contaminants. Resazurin dye was used in the study as an indicator in the determination of cell growth.[42] Oxidoreductases within viable cells reduced the resazurin salt to resorufin and changed the color from blue and non-fluorescent to pink and fluorescent.

The MBC is the lowest concentration of an anti-bacterial agent that totally kills a bacterium. For the MBC test, plating of a suspension from each well of the microtiter plates into MHA plates was accomplished, and the plates were incubated at 37 °C for 24 h. The lowest concentration with no noticeable growths on the MHA plate was considered to be the MBC value.

Fig. 10 shows the MICs and MBCs of the $MnAl_2O_4 \cdot ZnAl_2O_4$ nanomaterial against five different bacteria. The MIC is the

lowest concentration of the anti-bacterial agent to inhibit the growth of bacteria. As shown in Table 3, the MIC values of the $MnAl_2O_4 \cdot ZnAl_2O_4$ nanomaterial against the MDR pathogens ranged from 0.001 to 0.008 μg μL^{-1}. *E. coli* and *P. aeruginosa* showed MIC values of 0.002 μg μL^{-1}, while *S. aureus* showed 2 times lower MIC (0.001 μg μL^{-1}) than these two pathogens. *K. pneumoniae* showed an MIC of 0.004 μg μL^{-1}, while *P. mirabilis* showed a maximum MIC of 0.008 μg μL^{-1}.

The MBC is the lowest concentration of an antibacterial agent that kills a bacterium (shows no growth on the agar plate). In the present study, the MBC for *P. mirabilis* was a maximum of 0.016 μg μL^{-1}, while the lowest MBCs found in the cases of *S. aureus* (0.002 μg μL^{-1}). *E. coli*, and *P. aeruginosa* showed the same MBC value of 0.004 μg μL; meanwhile, *K. pneumoniae* showed an MBC of 0.008 μg μL^{-1}. Finally, the MIC and MBC values are indicative of the minimum efficient doses for bacteria killing as well as sterilizing effects by the $MnAl_2O_4 \cdot ZnAl_2O_4$ nanomaterial.[28,39]

Detection of 3-chlorophenol by $MnAl_2O_4 \cdot ZnAl_2O_4$ nanomaterials

The proposed chemical sensor was prepared by $MnAl_2O_4 \cdot ZnAl_2O_4$ nanomaterial/Nafion/GCE and employed to detect 3-CP successively in aqueous medium. The Nafion binder, which was suspended in ethanol as a 5% solution, was used to
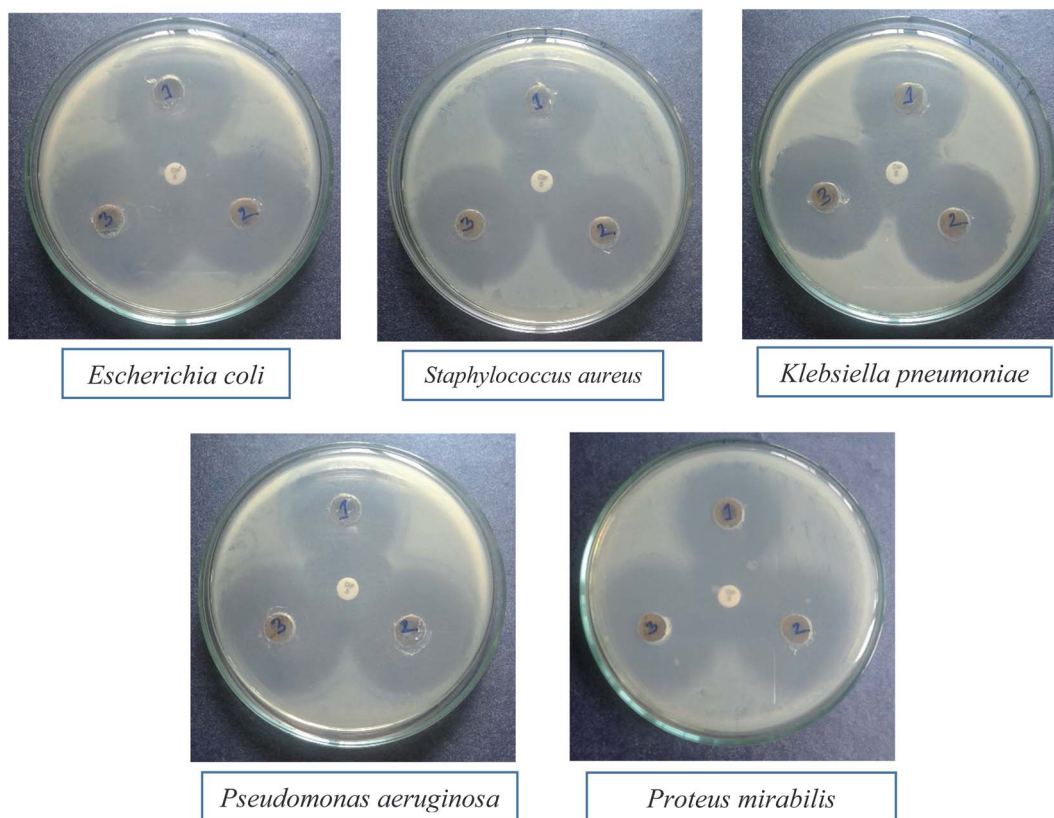
Fig. 9 *In vitro* anti-bacterial activity of the MnAl$_2$O$_4$·ZnAl$_2$O$_4$ nanomaterial against multidrug resistant "superbugs" in the presence of light (the middle spot shows the zone of inhibition by the GEN 10 standard).

Table 2 Comparison of the anti-bacterial activities of the MnAl$_2$O$_4$·ZnAl$_2$O$_4$ nanomaterial in the absence and presence of light

Isolates name	Zone of inhibition in absence of light (mm)			Zone of inhibition in presence of light (mm)		
	1 mg mL^{-1}	2 mg mL^{-1}	3 mg mL^{-1}	1 mg mL^{-1}	2 mg mL^{-1}	3 mg mL^{-1}
Escherichia coli	23	29	29	33	36	38
Staphylococcus aureus	27	28	30	30	33	35
Klebsiella pneumoniae	29	29	32	32	33	35
Pseudomonas aeruginosa	29	32	32	33	35	29
Proteus mirabilis	25	27	29	27	31	35
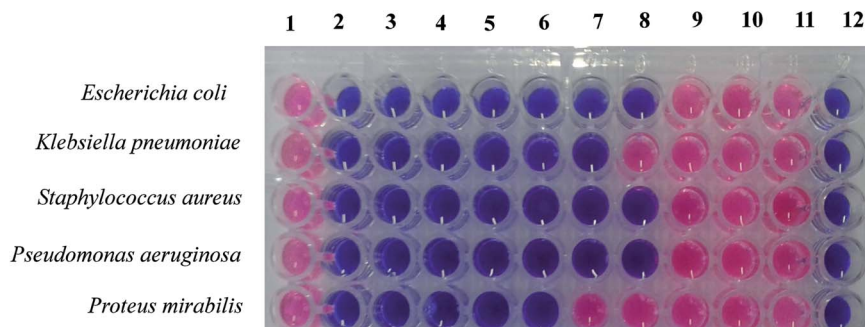
Fig. 10 Determination of the MIC and MBC values for the MnAl$_2$O$_4$·ZnAl$_2$O$_4$ nanomaterial against several bacterial pathogens with both Gram positive (*S. aureus*, *B. subtilis*) and Gram negative (*S. marcescens*, *E. coli*, *K. pneumoniae*, *P. aeruginosa*, *P. mirabilis*) bacteria.

Table 3 Evaluation of the MIC and MBC by the PrestoBlue-assisted microdilution approach of the $MnAl_2O_4 \cdot ZnAl_2O_4$ nanomaterial against five pathogenic bacteria

Isolates name	MIC (mg L^{-1})	MBC (mg L^{-1})
Escherichia coli	0.002	0.004
Staphylococcus aureus	0.001	0.002
Klebsiella pneumoniae	0.004	0.008
Pseudomonas aeruginosa	0.002	0.004
Proteus mirabilis	0.008	0.016

increase the binding strength between nanomaterials and GCE. As a result, the fabricated working electrode exhibited more stability, a modified electron transfer rate and high conductivity in aqueous detecting medium of 3-CP.[43,44] Thus, the prepared chemical sensor possessed high stability, enhanced electrochemical activity, and good sensitivity with a lower detection limit and, above all, safe chemo-characteristics. The $MnAl_2O_4 \cdot ZnAl_2O_4$ nanomaterial/Nafion/GCE assembly was implemented to detect the analyte 3-CP in buffer medium. In the detection of the target 3-CP, the current *versus* potential relation was used, as determined by an electrometer for the sensor probe $MnAl_2O_4 \cdot ZnAl_2O_4$ nanomaterial/Nafion/GCE in different electrochemical conditions, where the holding time was 1.0 s. The detection of the oxidation mechanism of 3-CP with the $MnAl_2O_4 \cdot ZnAl_2O_4$ nanomaterial/Nafion/GCE sensor probe is presented in Scheme 1.
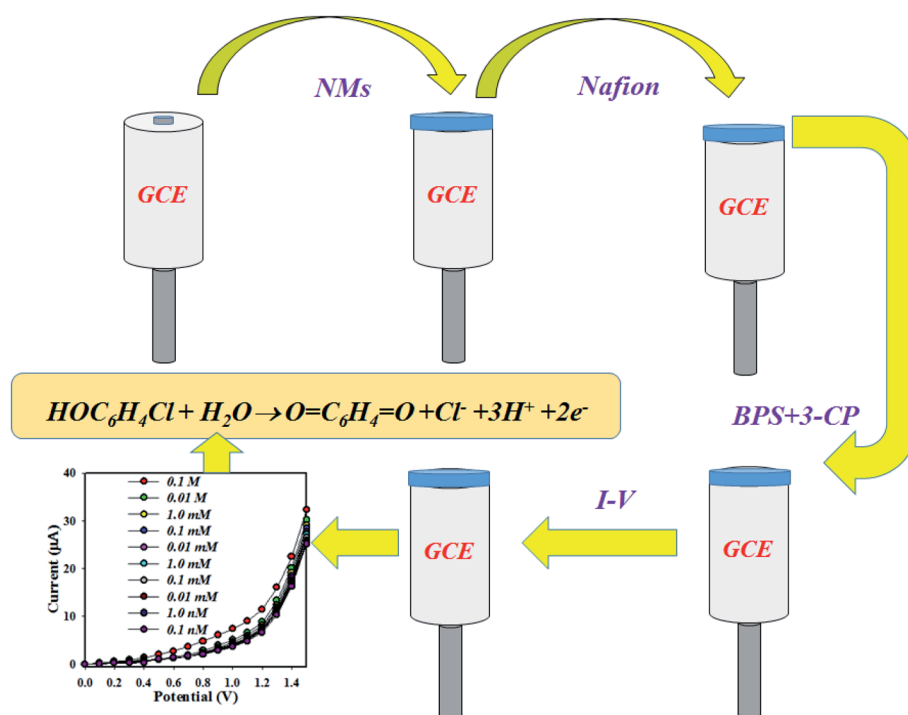
During 3-CP oxidation, the $MnAl_2O_4 \cdot ZnAl_2O_4$ nanomaterial/Nafion/GCE released electrons in the phosphate buffer phase.

The changes of the electrochemical current response were observed by an electrometer. In this approach, 3-CP and H_2O are adsorbed onto surface of $MnAl_2O_4 \cdot ZnAl_2O_4$ nanomaterial/Nafion/GCE sensor probe. Finally, quinone, hydrogen ions, chloride ions and electrons are produced on the surface, as shown in reaction (i).[45]

$$HOC_6H_4Cl + H_2O \rightarrow O{=}C_6H_4{=}O + Cl^- + 3H^+ + 2e^- \quad (i)$$
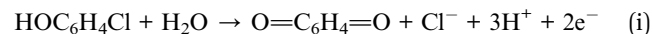
In reaction (i), the electrons were released by the chemical process. Therefore, the conductance of the $MnAl_2O_4 \cdot ZnAl_2O_4$ nanomaterial/Nafion/GCE working electrode significantly increased. This is the key reason for the enhanced current during the detection of the target analyte with the fabricated $MnAl_2O_4 \cdot ZnAl_2O_4$ nanomaterial/Nafion/GCE electrode in the electrochemical analysis.

To measure the selectivity of the proposed chemical sensor, a number of environmental toxins were evaluated at the concentration of 0.1 μM 3-CP and pH 7.0, and the responses of 2,4-DNP, 2-NP, 3-CP, 3-MP, 3-MPHyd, 4-NP, 4-AP, BPA, PHyd and *p*-NP are represented in Fig. 11(a). Evidently, 3-CP exhibited the maximum I–V response under the experimental conditions. The analytical performance of the proposed sensor, such as reproducibility, was obtained with 0.1 μM of 3-CP solution. As is represented in Fig. 11(b), the ten replicate runs in identical environments are indistinguishable. Thus, this experiment provides evidence of the reversibility of the 3-CP chemical sensor. Notably, the electrochemical response was not significantly changed even after washing several times with phosphate buffer phase after each reading. The standard deviation of reproducibility (RSD%) was calculated, and it was 3.06 for the

Scheme 1 The expected mechanism for the determination of 3-CP by the $MnAl_2O_4 \cdot ZnAl_2O_4$ nanomaterial/Nafion/GCE.

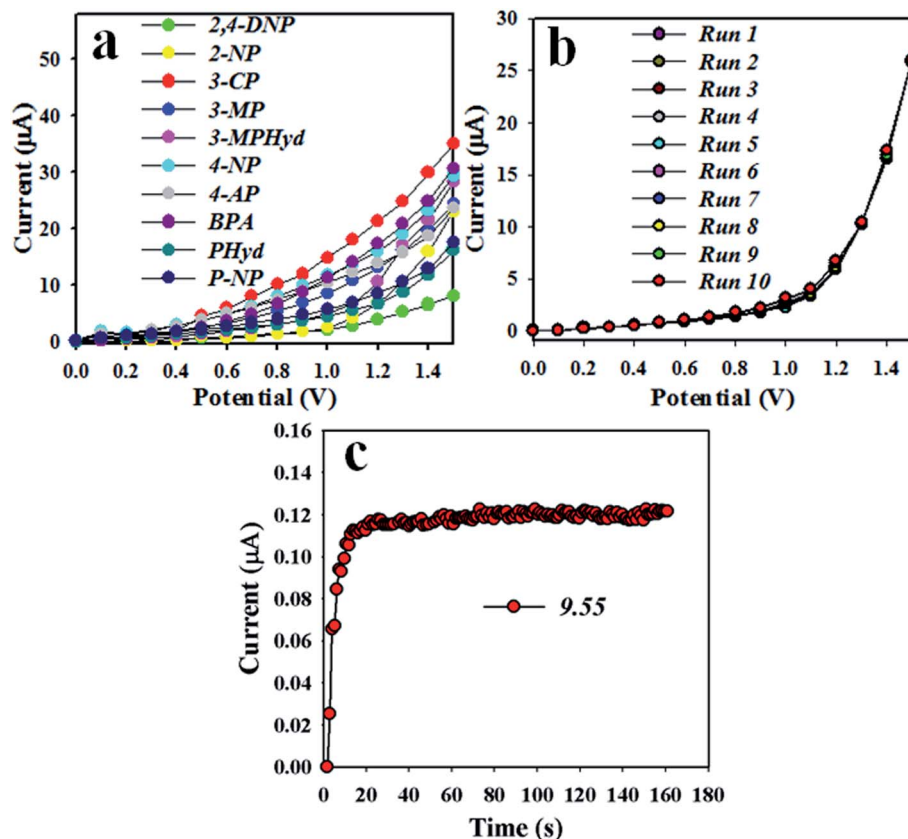**Fig. 11** Optimization of the 3-CP sensor based on the $MnAl_2O_4 \cdot ZnAl_2O_4$ nanomaterial: (a) selectivity, (b) repeatability, and (c) response time.

electrochemical observation. The sensor response time was also measured by an electrochemical process under identical conditions in 0.1 μM 3-CP at room conditions. The results are presented in Fig. 11(c), where the response time was found to be 10.0 s. It is considered that the sensor response is very fast. It is possible to detect the target chemical within a short span of time.

The electrochemical $I–V$ responses of 3-CP at different concentrations in the range of 0.1 nM to 0.1 M are illustrated in Fig. 12(a). This is a very wide range, as can be seen in Fig. 12(a), and the applied potential range is 0–1.5 V. To plot a calibration curve, the current data at a potential of +1.5 V were collected from Fig. 12(a) and plotted in Fig. 12(b) as the current *vs.* the concentration of 3-CP. The estimated regression coefficient of the calibration curve is equal to 0.9912. The sensitivity was calculated as 70.07 μA mM^{-1} cm^{-2}. The linearity of the curve was obtained over the LDR of 0.0 nM to 0.01 M. The LOD was calculated as 0.0014 ± 0.0001 nM, and the LOQ was calculated as 0.004 nM. Obviously, the proposed chemical sensor was implemented successively to detect 3-CP in phosphate buffer medium in a wide range of concentrations.

It can be observed that the electrochemical response is directly proportional to the concentration of the target 3-CP in the electrochemical system. Therefore, an enhanced electrochemical signal ($I–V$ response) was found with increasing target concentration of 3-CP. The same phenomenon for the current response with the concentration of the analyte was already reported in published papers.[46–48] Initially, in the

investigation of 3-CP, an exceedingly small number of 3-CP molecules are adsorbed onto the surface of the $MnAl_2O_4$-$\cdot ZnAl_2O_4$ nanomaterial/Nafion/GCE film, where the oxidation process is initiated significantly. Due to increasing of the target 3-CP concentration on the $MnAl_2O_4 \cdot ZnAl_2O_4$ nanomaterial/Nafion/GCE electrode surface of the chemical sensor, the chemical reaction significantly increased, where a larger active nanomaterial surface coverage with increased target 3-CP compound was achieved. Again, with enrichment of the 3-CP concentration, a highly intense electrochemical signal was obtained, and the maximum surface coverage was obtained by the corresponding analyte on the $MnAl_2O_4$-$\cdot ZnAl_2O_4$ nanomaterial/Nafion/GCE sensor. Further, upon increasing the target analyte 3-CP on the surface of the $MnAl_2O_4 \cdot ZnAl_2O_4$ nanomaterial/Nafion/GCE electrode, the surface coverage with 3-CP chemicals reached the saturation level. The substantial electrochemical result of the sensor response was achieved on the prepared $MnAl_2O_4 \cdot ZnAl_2O_4$ nanomaterial/Nafion/GCE sensor probe. Therefore, it is concluded that the chemical sensor based on the $MnAl_2O_4$-$\cdot ZnAl_2O_4$ nanomaterial/Nafion/GCE electrode can be applied for efficient detection of 3-CP. As is represented in Fig. 11(c), a ~10.0 s response time is estimated. Thus, 10.0 s is necessary to achieve steady state saturation by the proposed chemical sensor. Based on the analytical performance of the sensor, such as DL and LDR, the proposed 3-CP chemical sensor fabricated using $MnAl_2O_4 \cdot ZnAl_2O_4$ nanomaterial/Nafion/GCE
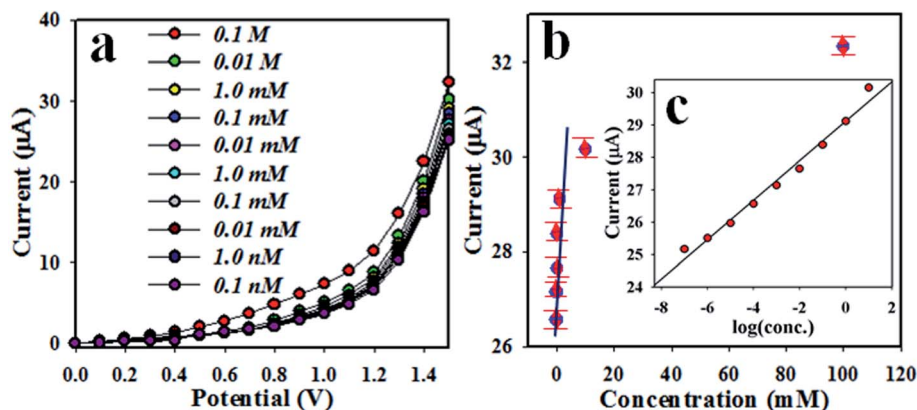
Paper

Fig. 12 (a) Concentration variation of the 3-CP chemical sensor based on the $MnAl_2O_4 \cdot ZnAl_2O_4$ nanomaterial by the electrochemical method and (b) calibration curve ((c) inset: log[3-CP conc.] *vs.* current).

Table 4 Comparison of the $MnAl_2O_4 \cdot ZnAl_2O_4$ nanomaterial/Nafion/GCE sensor performance with that of various electroanalytical methods at room conditions[a]

Electrode	Analyte	LDR(μM)	DL (μM)	Ref.
HRP/Au NPs/GCE	4-CP	2.5–117.5	0.39	49
CTAB-MMT/CPE	4-CP	0.05–10	0.02	50
TiO_2/GPE	4-CP	0.05–50	0.01	51
AB-DHP/GCE	2-CP	0.2–40	0.05	52
MWNTs-DCP1/GCE	2-CP	0.1–20	0.04	53
HRP/MWNTs/GCE	2,4-DCP	1.0–100	0.38	54
Tyrosinase/MWNTs/GCE	2,4-DCP	2.0–100	0.66	55
Nafion/MWCNT/GCE	2,4-DCP	0.1–100	0.037	56
MWCNT/EP/GCE	PCP	2–12	0.8	57
TiO_2/DHP/GCE	PCP	0.05–100	0.01	58
Graphene/HRP/GCE	2,4-DCP	0.01–13.0	0.005	59
$MnAl_2O_4 \cdot ZnAl_2O_4$/GCE	3-CP	0.0001–10000	0.0000014	This work

[a] DL (detection limit), LDR (linear dynamic range), μM (micromole), 3-CP (chlorophenol).

demonstrated highly qualified performance compared to chemical sensors formulated with the various nanostructured oxides of transition metals. A comparison of the sensor performance is presented in Table 4. Therefore, finally, the prepared 3-CP analyte is good and effective to detect 3-CP using current-*versus*-potential approaches. A detailed comparison of earlier tested 3-CP chemical sensors is presented in Table 4.[49–59]

Electrochemical characterization of the $MnAl_2O_4 \cdot ZnAl_2O_4$ nanomaterial/GCE probe

Here, the $MnAl_2O_4 \cdot ZnAl_2O_4$ nanomaterial/Nafion/GCE electrode was characterized using cyclic voltammetry (CV) and electrochemical impedance spectroscopy (EIS) techniques. The electrochemical redox as well as the impedance properties of $MnAl_2O_4 \cdot ZnAl_2O_4$ in the $MnAl_2O_4 \cdot ZnAl_2O_4$ nanomaterial/Nafion/GCE sensor probe were studied here for efficient detection by an electrochemical approach. In this analysis, we used a three-electrode system, where Ag/AgCl (sat. KCl), $MnAl_2O_4$-$\cdot ZnAl_2O_4$ nanomaterials/Nafion/GCE, and Pt were used as the reference, working and counter electrodes, respectively. The

cyclic voltametric response in the $[Fe(CN)_6]^{3-/4-}$ couple was found and is presented in Fig. 13(a). The electron transfer activity was investigated by CV within bare-GCE and coated-GCE in 5.0 mM $[Fe(CN)_6]^{3-/4-}$ couple, and the results are shown in Fig. 13(a). The coated-GCE showed well-distinguished redox peaks at +0.34 V and +0.13 V. Here, the bare-GCE showed weak CV-response in a similar electrochemical system compared to the coated-GCE electrode. This specifies that $MnAl_2O_4 \cdot ZnAl_2O_4$ nanomaterial/Nafion/GCE remarkably enhanced the electron transfer performance compared to bare-GCE.[60,61] This finding is corroborated by the outcomes of the acquired CVs, in which $MnAl_2O_4 \cdot ZnAl_2O_4$ nanomaterial/Nafion/GCE [Fig. 13(a) (redline)] exhibited higher conductance compared to bare GCE [Fig. 13(a) (blue-line)]. On the other hand, electrochemical impedance spectroscopy (EIS) is very good and efficient in assessing electron transfer mobility into electrode-solution interfaces as well as the resistivity of coated-GCE with respect to the resultant current. Therefore, EIS was used to further analyze the electrochemical behavior of bare-GCE as well as coated $MnAl_2O_4 \cdot ZnAl_2O_4$ nanomaterial/Nafion/GCE electrode. The faster electron transfer activity on the $MnAl_2O_4 \cdot ZnAl_2O_4$
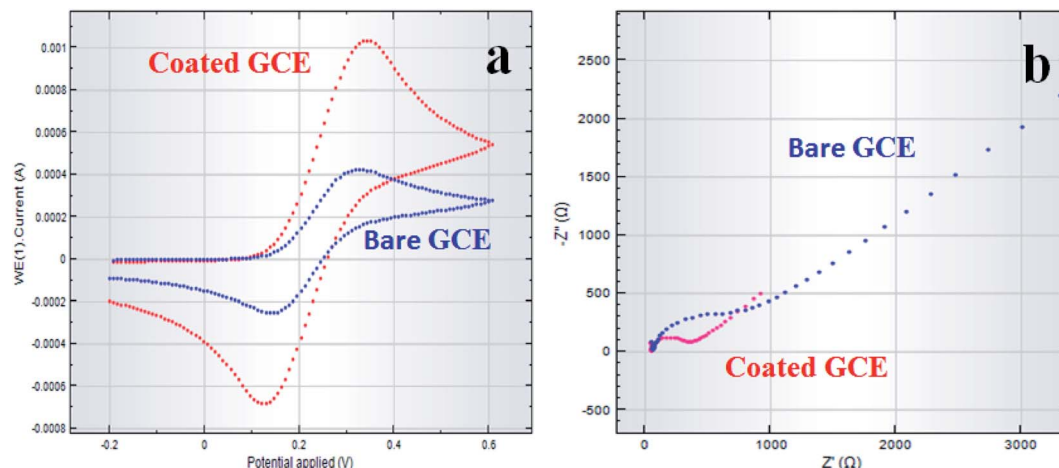
Fig. 13 Electrochemical characterization of $MnAl_2O_4 \cdot ZnAl_2O_4$ nanomaterial/Nafion/GCE. Comparison of (a) cyclic voltammetry and (b) Nyquist plots (EIS) of $MnAl_2O_4 \cdot ZnAl_2O_4$ nanomaterial/Nafion/GCE (red-line) and of bare GCE (blue-line) at pH 7.0 in 0.1 M PBS.

nanomaterial coated-GCE is expected, if the $MnAl_2O_4 \cdot ZnAl_2O_4$ nanomaterial coated-GCE is significant and efficient. In the EIS analysis, the diameter of the semicircle indicates the effective charge-transfer resistances (R_{CT}) of the uncoated electrode and that coated with $MnAl_2O_4 \cdot ZnAl_2O_4$ nanomaterial.[62,63] It is presented in Fig. 13(b) that the bare-GCE electrode showed higher resistance compared to the $MnAl_2O_4 \cdot ZnAl_2O_4$ nanomaterial-coated GCE under identical conditions. This shows that the coated GCE has significantly improved charge-transfer ability compared to the bare electrode. It is also indicated that the conductivity of the $MnAl_2O_4 \cdot ZnAl_2O_4$ nanomaterial-coated GCE has significantly improved owing to the enhanced electron transfer properties.[64,65] Finally, the complex plane plots are presented in Fig. 13(b) (red line), which displays the results for the 0.1 M PBS/$K_3[Fe(CN)_6]$ electrochemical system. The $MnAl_2O_4 \cdot ZnAl_2O_4$ nanomaterial-coated GCE showed lower impedance (lower capacitive current) (R_{CT}: 347 Ω) compared to bare GCE (R_{CT}: 816 Ω) electrode [Fig. 13(b) (blue-line)]. The lower capacitive current with less impedance of the $MnAl_2O_4 \cdot ZnAl_2O_4$ nanomaterial/Nafion/GCE sensor probe suggests that the

electron-transfer ability of the coated-GCE electrode was improved in the presence of a ternary mixed $MnAl_2O_4 \cdot ZnAl_2O_4$ nanomaterial coating. The $MnAl_2O_4 \cdot ZnAl_2O_4$ material was bonded with Nafion onto the GCE surface. Finally, this electro-active property of the coated GCE suggests that the fabricated $MnAl_2O_4 \cdot ZnAl_2O_4$ nanomaterial-coated sensor probe has significantly improved electro-chemical activity during EIS analysis (Fig. 13(b)).

Real sample analysis

For validation, the fabricated $MnAl_2O_4 \cdot ZnAl_2O_4$ nanomaterial/Nafion/GCE sensor probe was used to detect the target 3-CP in real environmental and extracted samples from practical environmental fields.[41] Extracted and collected samples, including industrial effluent and extracts from a PC baby-bottle, PC water-bottle and PVC food packaging bag, were used in the analysis for the justification of the fabricated $MnAl_2O_4 \cdot ZnAl_2O_4$ nanomaterial/Nafion/GCE sensor probe. The results of the analysis are depicted in Table 5. We found good and acceptable results.

Table 5 Validation of the $MnAl_2O_4 \cdot ZnAl_2O_4$ nanomaterial/Nafion/GCE sensor probe for the detection of 3-CP in various real samples by an electrochemical approach

Sample	Added 3-CP conc. (μM)	Determined 3-CP conc. by $MnAl_2O_4 \cdot ZnAl_2O_4$ nanomaterial (μM)	Recovery (%)	RSD (%) ($n = 3$)
Industrial effluent	0.0100	0.0111	111	2.27
	0.0100	0.0113	113	
	0.0100	0.0108	108	
PC baby bottle	0.0100	0.0096	96	0.60
	0.0100	0.0097	97	
	0.0100	0.0097	97	
PC water bottle	0.0100	0.0099	99	0.58
	0.0100	0.0099	99	
	0.0100	0.0100	100	
PVC food packaging bag	0.0100	0.0096	96	1.03
	0.0100	0.0097	97	
	0.0100	0.0098	98	

© 2021 The Author(s). Published by the Royal Society of Chemistry

Conclusion

In summary, a facile synthetic method in aqueous medium has been demonstrated for the synthesis of a $MnAl_2O_4 \cdot ZnAl_2O_4$ nanomaterial, and it has been applied as an efficient photocatalyst, MDR anti-bacterial agent and 3-CP sensor. The nanomaterial was characterized by XRD, SEM, EDS, TEM, AFM, FTIR, PL, CV and EIS spectroscopy. The average crystallite size of the synthesized nanomaterial was found to be 48.5 nm from XRD. Diverse PL properties were observed for mono-, di- and trimetallic oxides, where the $MnAl_2O_4 \cdot ZnAl_2O_4$ nanomaterial showed relatively reduced PL intensity that is suitable for preventing electron–hole recombination. The photocatalytic efficiency at pH 9 was 71% for the catalyst only and increased to 91% when the catalyst promoter H_2O_2 was used with $MnAl_2O_4 \cdot ZnAl_2O_4$ at the same pH. The results revealed enhanced anti-bacterial performance of $MnAl_2O_4 \cdot ZnAl_2O_4$ against MDR bacteria both in the absence and presence of light compared to the standard GEN 10 antibiotic, with a greater effect in the presence of light through the ROS mechanism and mechanical damage of bacteria. These results indicate excellent sterilizing properties of the $MnAl_2O_4 \cdot ZnAl_2O_4$ nanomaterial for industrial and biomedical applications.

The proposed 3-CP chemical sensor with the $MnAl_2O_4 \cdot ZnAl_2O_4$ nanomaterial exhibited higher sensitivity, the lowest detection limit, long term stability and enhanced electrochemical responses by the proposed electrochemical method. The calibration plot is linear over the concentration range in the LDR. The sensitivity of the sensor was calculated as 70.07 µA mM^{-1} cm^{-2} with a DL of 0.0014 ± 0.0001 nM from the calibration plot of the LDR. This introduces a new route for the development of selective and sensitive chemical sensors for the environmental safety and healthcare arenas in an extensive range.

Conflicts of interest

There are no conflicts to declare.

Acknowledgements

References

1 R. Cao, W. X. Pan and G. L. Griffin, Direct synthesis of higher alcohols using bimetallic copper/cobalt catalysts, *Langmuir*, 1988, **4**(5), 1108–1112.

2 G. R. Sheffer, R. A. Jacobson and T. S. King, Chemical nature of alkali-promoted copper-cobalt-chromium oxide higher alcohol catalysts, *J. Catal.*, 1989, **116**(1), 95–107.

3 A. J. Marchi, J. I. Di Cosimo and C. R. Apesteguía, Effect of the preparation conditions on the reducibility of Cu-Co based oxides, *Catal. Today*, 1992, **15**(3–4), 383–394.

4 G. Fornasari, A. D. Huysser and L. Mintchev, F. and A. TriÐroVaccari, *J. Catal.*, 1992, **135**, 386.

5 R. T. Figueiredo, M. L. Granados, J. L. G. Fierro, L. Vigas, P. R. de la Piscina and N. Homs, Preparation of alumina supported CuCo catalysts from cyanide complexes and their performance in CO hydrogenation, *Appl. Catal., A*, 1998, **170**(1), 145–157.

6 A. D. de Aquino and A. J. G. Cobo, Synthesis of higher alcohols with cobalt and copper-based model catalysts: effect of the alkaline metals, *Catal. Today*, 2001, **65**(2–4), 209–216.

7 L. Sujun, Synthesis and application of Manganese oxide-based nanomaterials, *Adv. Mater. Res.*, 2014, **830**, 33–36.

8 J. Theerthagiri, S. Salla, R. A. Senthil, *et al.*, A review on ZnO nanostructured materials: energy, environmental and biological applications, *Nanotechnology*, 2019, **30**, 392001.

9 A. F. Osama, S. K. Abd El Rahman, D. M. Qilin and E. Samy, Structural and catalytic properties of ZnO and Al_2O_3 nanostructures loaded with metal nanoparticles, *J. Nanopart. Res.*, 2011, **13**, 7075–7083.

10 K. Zhu, C. Liu, X. Ye and Y. Wu, Catalysis of hydrotalcite-like compounds in liquid phase oxidation:(I) phenol hydroxylation, *Appl. Catal., A*, 1998, **168**(2), 365–372.

11 F. Trifirò, A. Vaccari and F. Cavani, Hydrotalcite-type anionic clays: preparation, properties and applications, *Catal. Today*, 1991, **11**, 173–302.

12 Y. M. Liu, S. T. Liu, K. Z. Zhu, X. K. Ye and Y. Wu, Catalysis of hydrotalcite-like compounds in liquid phase oxidation:(II)-Oxidation of p-cresol to p-hydroxybenzaldehyde, *Appl. Catal., A*, 1998, **169**(1), 127–135.

13 T. Mathew, N. R. Shiju, K. Sreekumar, B. S. Rao and C. S. Gopinath, Cu–Co synergism in $Cu_{1-x}Co_xFe_2O_4$-catalysis and XPS aspects, *J. Catal.*, 2002, **210**(2), 405–417.

14 I. E. Wachs, Recent conceptual advances in the catalysis science of mixed metal oxide catalytic materials, *Catal. Today*, 2005, **100**(1–2), 79–94.

15 M. A. Subhan, P. C. Saha, M. M. Rahman, M. A. R. Akand, A. M. Asiri and M. Al-Mamun, Enhanced photocatalytic activity and chemical sensor development based on ternary $B_2O_3 \cdot Zn_6Al_2O_9 \cdot ZnO$ nanomaterials for environmental safety, *New J. Chem.*, 2017, **41**(15), 7220–7231.

16 J. Michałowicz and W. Duda, Phenols-Sources and Toxicity, *Pol. J. Environ. Stud.*, 2007, **16**(3), 347–362.

17 D. Wei, T. Kameya and K. Urano, Environmental management of pesticidal POPs in China: past, present and future, *Environ. Int.*, 2007, **33**(7), 894–902.

18 Q. Xu, X. Li, Y. E. Zhou, H. Wei, X. Y. Hu, Y. Wang and Z. Yang, An enzymatic amplified system for the detection of 2, 4-dichlorophenol based on graphene membrane modified electrode, *Anal. Methods*, 2012, **4**(10), 3429–3435.

19 L. Keith and W. Telliard, ES&T special report: priority pollutants: Ia perspective view, *Environ. Sci. Technol.*, 1979, **13**(4), 416–423.

20 M. M. Rahman, T. A. Sheikh, A. M. Asiri and M. R. Awual, Development of 3-methoxyaniline sensor probe based on thin $Ag_2O@La_2O_3$ nanosheets for environmental safety, *New J. Chem.*, 2019, **43**, 4620–4632.

21 M. M. Rahman, M. M. Hussain, M. N. Arshad, M. R. Awual and A. M. Asiri, Arsenic sensor development based on modification with (E)-N′-(2-nitrobenzylidine)-benzenesulfonohydrazide: a real sample analysis, *New J. Chem.*, 2019, **43**, 9066–9075.

22 T. A. Sheikh, M. M. Rahman, A. M. Asiri, H. M. Marwani and M. R. Awual, 4-Hexylresorcinol sensor development based on wet-chemically prepared $Co_3O_4@Er_2O_3$ nanorods: A practical approach, *J. Ind. Eng. Chem.*, 2018, **66**, 446–455.

23 L. Guo and H. K. Lee, Electro membrane extraction followed by low-density solvent-based ultrasound-assisted emulsification microextraction combined with derivatization for determining chlorophenols and analysis by gas chromatography–mass spectrometry, *J. Chromatogr. A*, 2012, **1243**, 14–22.

24 Y. Y. Chao, Y. M. Tu, Z. X. Jian, H. W. Wang and Y. L. Huang, Direct determination of chlorophenols in water samples through ultrasound-assisted hollow fiber liquid–liquid–liquid microextraction on-line coupled with high-performance liquid chromatography, *J. Chromatogr. A*, 2013, **1271**(1), 41–49.

25 M. F. Pistonesi, M. S. Di Nezio, M. E. Centurión, M. E. Palomeque, A. G. Lista and B. S. F. Band, Determination of phenol, resorcinol and hydroquinone in air samples by synchronous fluorescence using partial least-squares (PLS), *Talanta*, 2006, **69**(5), 1265–1268.

26 L. H. Zhang, C. J. Zhang, X. Chen, Y. Q. Feng and X. Z. Wu, In-capillary solid-phase extraction–capillary electrophoresis for the determination of chlorophenols in water, *Electrophoresis*, 2006, **27**(16), 3224–3232.

27 S. Zhang, Z. Shi, J. Wang, Q. Cheng and K. Wu, Preparation of three-dimensionally ordered macroporous polycysteine film and application in sensitive detection of 4-chlorophenol, *Electrochim. Acta*, 2014, **130**, 734–739.

28 M. A. Subhan, S. S. Jhuma, P. C. Saha, M. M. Alam, A. M. Asiri, M. Al-Mamun and M. M. Rahman, Efficient selective 4-aminophenol sensing and antibacterial activity of ternary $Ag_2O_3 \cdot SnO_2 \cdot Cr_2O_3$ nanoparticles, *New J. Chem.*, 2019, **43**(26), 10352–10365.

29 G. N. Rani and N. H. Ayachit, Low temperature synthesis of $MgAl2O4$ Spinel through sol-gel technique and its characterization, *Can. J. Phys.*, 2015, **93**(5), 561–564.

30 Z. Zhu, Q. Zhao, X. Li, H. Li, M. Tade and S. Liu, Photocatalytic performances and activities in Ag-doped $ZnAl_2O_4$ nanorods studied by FTIR spectroscopy, *Catal. Sci. Technol.*, 2013, **3**(3), 788–796.

31 S. Iaiche and A. Djelloul, $ZnO/ZnAl_2O_4$ nanocomposite films studied by X-ray diffraction, FTIR, and X-ray photoelectron spectroscopy, *J. Spectrosc.*, 2015, 2015.

32 S. Li, Removal of crystal violet from aqueous solution by sorption into semi-interpenetrated networks hydrogels constituted of poly(acrylic acid-acrylamide-methacrylate) and amylose, *Bioresour. Technol.*, 2010, **101**(7), 2197–2202.

33 G. Favaro, D. Confortin, P. Pastore and M. Brustolon, Application of LC-MS and LC-MS-MS to the analysis of photo-decomposed crystal violet in the investigation of cultural heritage materials aging, *J. Mass Spectrom.*, 2012, **47**, 1660–1670.

34 M. A. Subhan, P. C. Saha, M. A. Hossain, *et al.*, Photocatalysis, photoinduced enhanced antibacterial functions and development of a selective m-tolyl hydrazine sensor based on mixed $Ag \cdot NiMn_2O_4$ nanomaterials, *RSC Adv.*, 2020, **10**, 30603.

35 M. A. Subhan, T. P. Rifat, P. C. Saha, *et al.*, Photocatalytic, anti-bacterial performance and development of 2,4-diaminophenylhydrazine chemical sensor probe based on ternary doped $Ag \cdot SrSnO_3$ nanorods, *New J. Chem.*, 2021, **45**(3), 1634–1650.

36 M. A. Subhan, P. C. Saha, J. Ahmed, A. M. Asiri, M. Al-Mamun and M. M. Rahman, Development of ultra-sensitive para-nitrophenol sensor using a tri-metalllic oxide $MoO_2 \cdot Fe_3O_4 \cdot CuO$ nanocomposites, *Mater. Adv.*, 2020, **1**, 2831.

37 L. Zhang, Y. Jiang, Y. Ding, M. Povey and D. York, Investigation into the antibacterial behaviour of suspensions of ZnO nanoparticles (ZnO nanofluids), *J. Nanoparticle Res.*, 2007, **9**(3), 479–489.

38 N. Talebian, S. M. Amininezhad and M. Doudi, Controllable synthesis of ZnO nanoparticles and their morphology-dependent antibacterial and optical properties, *J. Photochem. Photobiol., B*, 2013, **120**, 66–73.

39 M. A. Subhan, T. P. Rifat, P. C. Saha, M. M. Alam, A. M. Asiri, M. M. Rahman and J. Uddin, Enhanced visible light-mediated photocatalysis, antibacterial functions and fabrication of a 3-chlorophenol sensor based on ternary $Ag_2O \cdot SrO \cdot CaO$, *RSC Adv.*, 2020, **10**(19), 11274–11291.

40 J. McFarland, The nephelometer: an instrument for estimating the number of bacteria in suspensions used for calculating the opsonic index and for vaccines, *J. Am. Med. Assoc.*, 1907, **49**(14), 1176–1178.

41 M. A. Subhan, S. S. Jhuma, P. C. Saha, *et al.*, Photocatalysis, enhanced anti-bacterial performance and discerning thiourea sensing of $Ag_2O \cdot SnO_2 \cdot TiO_2$ hetero-structure, *J. Environ. Chem. Eng.*, 2020, **8**, 104051.

42 B. P. McNicholl, J. W. McGrath and J. P. Quinn, Development and application of a resazurin-based biomass activity test for activated sludge plant management, *Water Res.*, 2007, **41**(1), 127–133.

43 M. M. Alam, M. T. Uddin, A. M. Asiri, M. R. Awual and M. M. Rahman, Detection of uric acid based on doped $ZnO/Ag_2O/Co_3O_4$ nanoparticle loaded glassy carbon electrode, *New J. Chem.*, 2019, **43**, 8651–8659.

44 T. A. Sheikh, M. N. Arshad, M. M. Rahman, A. M. Asiri, H. M. Marwani, M. R. Awual and W. A. Bawazir, Trace electrochemical detection of Ni^{2+} ions with bidentate N, N′-(ethane-1,2-diyl)bis(3,4-dimethoxybenzenesulfonamide)
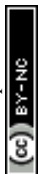
[EDBDMBS] as a chelating agent, *Inorg. Chim. Acta*, 2017, **464**, 157–166.

45 M. M. Alam, A. M. Asiri, M. T. Uddin, M. A. Islam, M. R. Awual and M. M. Rahman, One-step wet-chemical synthesis of ternary ZnO/CuO/Co3O4 nanoparticles for sensitive and selective melamine sensor development, *New J. Chem.*, 2019, **43**, 4849–4858.

46 M. M. Rahman, M. M. Alam, A. M. Asiri and M. A. Islam, Fabrication of selective chemical sensor with ternary ZnO/SnO$_2$/Yb$_2$O$_3$ nanoparticles, *Talanta*, 2017, **170**, 215–223.

47 M. M. Rahman, M. M. Alam, A. M. Asiri and M. A. Islam, Ethanol sensor development based on ternary-doped metal oxides (CdO/ZnO/Yb$_2$O$_3$) nanosheets for environmental safety, *RSC Adv.*, 2017, **7**(37), 22627–22639.

48 M. M. Rahman, B. M. Abu-Zied, M. M. Hasan, A. M. Asiri and M. A. Hasnat, Fabrication of a selective 4-amino phenol sensor based on H-ZSM-5 zeolites deposited silver electrodes, *RSC Adv.*, 2016, **6**(54), 48435–48444.

49 C. Qiu, T. Chen, X. Wang, Y. Li and H. Ma, Application of horseradish peroxidase modified nanostructured Au thin films for the amperometric detection of 4-chlorophenol, *Colloids Surf., B*, 2013, **103**, 129–135.

50 H. Yang, X. Zheng, W. Huang and K. Wu, Modification of montmorillonite with cationic surfactant and application in electrochemical determination of 4-chlorophenol, *Colloids Surf., B*, 2008, **65**(2), 281–284.

51 C. Wan, Y. Zhang, H. Lin, K. Wu, J. Chen and Y. Zhou, Electrochemical determination of p-chlorophenol based on the surface enhancement effects of mesoporous TiO$_2$-modified electrode, *J. Electrochem. Soc.*, 2009, **156**(11), F151.

52 D. Sun and H. Zhang, Electrochemical determination of 2-chlorophenol using an acetylene black film modified glassy carbon electrode, *Water Res.*, 2006, **40**(16), 3069–3074.

53 C. Li, Voltammetric determination of 2-chlorophenol using a glassy carbon electrode coated with multi-wall carbon nanotube-dicetyl phosphate film, *Microchim. Acta*, 2007, **157**(1–2), 21–26.

54 S. Huang, Y. Qu, R. Li, J. Shen and L. Zhu, Biosensor based on horseradish peroxidase modified carbon nanotubes for determination of 2, 4- dichlorophenol, *Microchim. Acta*, 2008, **162**(1–2), 261–268.

55 L. Kong, S. Huang, Z. Yue, B. Peng, M. Li and J. Zhang, Sensitive mediator- free tyrosinase biosensor for the determination of 2, 4-dichlorophenol, *Microchim. Acta*, 2009, **165**(1–2), 203–209.

56 A. S. Arribas, M. Moreno, E. Bermejo, J. A. Pérez, V. Román, A. Zapardiel and M. Chicharro, Application of Carbon Nanotube-Modified Electrodes as Electrochemical Sensors for the Continuous Monitoring of 2,4-Dichlorophenol, *Electroanalysis*, 2011, **23**(1), 237–244.

57 A. Remes, A. Pop, F. Manea, A. Baciu, S. J. Picken and J. Schoonman, Electrochemical determination of pentachlorophenol in water on a multi-wall carbon nanotubes-epoxy composite electrode, *Sensors*, 2012, **12**(6), 7033–7046.

58 Y. Wu, Nano-TiO$_2$/dihexadecylphosphate based electrochemical sensor for sensitive determination of pentachlorophenol, *Sens. Actuators, B*, 2009, **137**(1), 180–184.

59 Q. Xu, X. Li, Y. E. Zhou, H. Wei, X. Y. Hu, Y. Wang and Z. Yang, An enzymatic amplified system for the detection of 2, 4-dichlorophenol based on graphene membrane modified electrode, *Anal. Methods*, 2012, **4**(10), 3429–3435.

60 M. Tertiș, A. Florea, A. Adumitrăchioaie, A. Cernat, D. Bogdan, L. Barbu-Tudoran, N. Jaffrezic Renault, R. Săndulescu and C. Cristea, Detection of Dopamine by a Biomimetic Electrochemical Sensor Based on Polythioaniline-Bridged Gold Nanoparticles, *Chempluschem*, 2017, **82**, 561–569.

61 M. S. Alam, M. M. Rahman, H. M. Marwani and M. A. Hasnat, Insights of temperature dependent catalysis and kinetics of electro-oxidation of nitrite ions on a glassy carbon electrode, *Electrochim. Acta*, 2020, **362**, 137102.

62 T. Alizadeh and S. Azizi, Graphene/graphite paste electrode incorporated with molecularly imprinted polymer nanoparticles as a novel sensor for differential pulse voltammetry determination of fluoxetine, *Biosens. Bioelectron.*, 2016, **81**, 198–206.

63 Z. Mumtarin, M. M. Rahman, H. M. Marwani and M. A. Hasnat, Electro-kinetics of conversion of NO$_3^-$ into NO$_2^-$ and sensing of nitrate ions via reduction reactions at copper immobilized platinum surface in the neutral medium, *Electrochim. Acta*, 2020, **346**, 135994.

64 K. Huo, Y. Li, R. Chen, B. Gao, C. Peng, W. Zhang, L. Hu, X. Zhang and P. K. Chu, Recyclable Non-Enzymatic Glucose Sensor Based on Ni/NiTiO$_3$/TiO$_2$ Nanotube Arrays, *ChemPlusChem*, 2015, **80**, 576–582.

65 Z. Mumtarin, M. M. Rahman and M. A. Hasnat, Electrocatalytic reduction of hydroxylamine on copper immobilized platinum surface: heterogeneous kinetics and sensing performance, *Electrochim. Acta*, 2019, **318**, 486–495.